1 **Tumor-educated Gr1+CD11b+ cells instigate breast cancer metastasis by twisting**

2 **cancer cells plasticity via OSM/IL6–JAK signaling**

3

4 Sanam Peyvandi[1, +, *], Manon Bulliard[1, +], Annamaria Kauzlaric[2], Oriana Coquoz[1], Yu-Ting

5 Huang[1], Nathalie Duffey[1, +], Laetitia Gafner[1], Girieca Lorusso[1], Nadine Fournier[2], Qiang

6 Lan[1,3,*,#], and Curzio Rüegg[1,*,#]

7

8 [1] Pathology Unit, Department of Oncology, Microbiology and Immunology (OMI), Faculty

9 of Science and Medicine, University of Fribourg, 1700 Fribourg, Switzerland;

10 [2] Translational Data Science Group, Swiss Institute of Bioinformatics, Lausanne,

11 Switzerland;

12 [3] Cell and Tissue Dynamics Research Program, Institute of Biotechnology, Helsinki

13 Institute of Life Science (HiLIFE), University of Helsinki, Helsinki, Finland.

14

15 * These authors contributed equally as corresponding authors.

16

17 + Current affiliations: S.P., Immunobiology Department, University of Lausanne (UNIL),

18 Switzerland; M.B., Swiss Institute for Experimental Cancer Research (ISREC), Ecole

19 Polytechnique Fédérale Lausanne (EPFL) UPCDA SV 2833 (Bâtiment SV) Lausanne,

20 Switzerland; N.D., Department of Oncology, Centre Hospitalier Universitaire Vaudois

21 (CHUV), University of Lausanne (UNIL), Switzerland; Y-T.H., Daiichi Sankyo Co., Ltd.

22 Taipei City, Taiwan

23

24 # Lead contacts and co-senior authors:

25   # C.R. (curzio.ruegg@unifr.ch; +4126 300 8766), Department of Oncology, Microbiology,

26   Immunology, Faculty of Science and Medicine, University of Fribourg, Chemin du Musée

27   18, Per 17, CH-1700 Fribourg, Switzerland

28   # Q.L. (qiang.lan@helsinki.fi) Cell and Tissue Dynamics Research Program, Institute of

29   Biotechnology, Helsinki Institute of Life Science (HiLIFE), Biocenter 2, P.O. Box 56,

30   FIN-00014, University of Helsinki, Helsinki, Finland

31

32   **Conflict-of-interests:** The authors have no conflicts of interest to declare.

33   **Running title:** OMS/IL6 twist breast cancer plasticity to promote metastasis

34   **Keywords:** Breast cancer metastasis, chemotherapy, cancer stem cells, GR1, Oncostatin

35   M, IL6, JAK, plasticity, heterogeneity

36

Abstract

Cancer cell plasticity contributes to tumor therapy resistance and metastasis formation, which represent the main causes of cancer-related death for most cancers, including breast cancer. The tumor microenvironment drives cancer cell plasticity and metastasis and, thus, unravelling the underlying cues may provide novel effective strategies to manage metastatic disease. Here, we show that stem cell antigen-1 positive (Sca-1$^+$) murine breast cancer cells enriched during tumor progression and metastasis have higher *in vitro* cancer stem cell-like properties, enhanced *in vivo* metastatic ability, and initiate primary tumors rich in Gr1^{high}CD11b$^+$Ly6C^{low} cells. In turn, tumor-educated Gr1$^+$CD11b$^+$ (Tu-Gr1$^+$CD11b$^+$) cells rapidly and transiently convert low metastatic 4T1-Sca-1$^-$ cells into highly metastatic 4T1-Sca-1$^+$ cells via secreted OSM and IL6. Moreover, chemotherapy-resistant and highly metastatic 4T1-derived cells maintain high Sca-1$^+$ frequency through cell autonomous IL6 production. Inhibition of OSM, IL6 or JAK suppressed Tu-Gr1$^+$CD11b$^+$-induced Sca-1$^+$ population enrichment *in vitro*, while JAK inhibition abrogated metastasis of chemotherapy-enriched Sca-1$^+$ cells *in vivo*. Importantly, Tu-Gr1$^+$CD11b$^+$ cells invoked a gene signature in tumor cells predicting shorter OS and RFS in breast cancer patients. Collectively, our data identified OSM/IL6-JAK as a clinically relevant paracrine/autocrine axis instigating breast cancer cell plasticity triggering metastasis.

Introduction

Metastasis accounts for over 90% of cancer-related death, calling for new strategies to prevent cancer cell dissemination and metastasis formation (1). Recent studies using single-cell lineage tracing and single-cell RNA sequencing (scRNA-seq) technologies have provided detailed information about intratumor heterogeneity (2, 3), whereby genetically, epigenetically and functionally diverse subpopulations of cancer cells exist within the tumor mass, spatially and temporally (4). Intratumor heterogeneity may arise by modulating cancer cell plasticity, especially of cancer stem cells (CSCs), through cell-intrinsic and -extrinsic mechanisms (5, 6).

Multiple CSC subpopulations appear to co-exist within the primary tumor mass resulting in high degree of tumor cell heterogeneity and increased aggressiveness (7) including in breast cancer (4, 8–11). In particular, CSCs can acquire metastasis initiating capacities (12) and resistance to therapy, resulting in cancer relapse (4). Moreover, non-CSCs within the tumor bulk may acquire CSC properties to repopulate the tumor(4). While CSC are defined rather functionally by their ability to initiate tumors and metastasis in low number *in vivo*, several cell surface markers associated with CSC features have been reported, including CD44, CD24, Sca-1, CD61, CD49f were used to identify breast CSCs (13, 14).

The interaction of tumor cells with the tumor microenvironment (TME) contributes to tumor cell plasticity and tumor heterogeneity (15, 16). Cells of the TME also promote tumor escape and metastasis through multiple mechanisms, including promotion of angiogenesis, cell survival, invasion, epithelial-mesenchymal transition (EMT), and immunosuppression (17–22). Recently, they have been reported to instigate expansion of CSC with metastatic ability (also known as metastasis-initiating cells) in different cancers (17, 23, 24). Thus, the TME dynamics is a key driver of cancer cell plasticity and

81 heterogeneity promoting tumor growth, progression and metastasis (4). Accurate

82 characterization of the regulation of tumor plasticity and heterogeneity by the TME may

83 reveal novel opportunities for developing effective anti-metastatic therapies (8, 14).

84 TME-derived Oncostatin M (OSM) has been shown to mediate tumor progression

85 and CSC stemness by activating its receptor OSMR (25). OSM belongs to the IL6 family

86 of cytokines (including IL6 itself, IL11 and LIF) (26, 27), whose members bind to dimeric

87 receptors sharing a common subunit (gp130 or IL6ST) and activate JAK-STAT, RAS-

88 MAPK and PI3K-AKT pathways (28, 29). Increased OSM or IL6 expression correlates with

89 reduced survival in breast cancer patients (30, 31). OSM was shown to drive breast cancer

90 progression and metastasis through direct effects on cancer cells, such as suppression of

91 estrogen receptor (ER) expression (31) and promotion of EMT (25, 32), and indirect effects

92 via TME cells, in particular the reprogramming of tumor associated macrophages and

93 fibroblasts (33–36).

94 Here, by assessing the metastatic evolution of murine triple-negative breast cancer

95 (TNBC) models *in silico* and *in vivo*, we observed that the Sca-1$^+$ tumor cell subpopulation

96 is enriched during tumor progression. We show that tumor-educated Gr1$^+$CD11b$^+$ cells

97 (Tu-Gr1$^+$CD11b$^+$), but not naïve Gr1$^+$CD11b$^+$ cells from spleen (Spl-Gr1$^+$CD11b$^+$) or bone

98 marrow (BM-Gr1$^+$CD11b$^+$) in tumor-bearing mice, modulate tumor plasticity via OSM/IL6-

99 JAK signaling by rapidly and transiently converting 4T1-Sca-1$^-$ cells into 4T1-Sca-1$^+$ cells

100 with high metastatic capacity. Prolonged exposure of 4T1 cells to chemotherapy stably

101 enriched for metastatic Sca-1$^+$ cells via an autocrine IL6-JAK signaling loop. A short *in vitro*

102 treatment of these chemo-resistant cells with the JAK inhibitor Ruxolitinib, suppressed their

103 metastatic capacity. Importantly, Tu-Gr1$^+$CD11b$^+$ invoked a gene expression signature in

104 4T1 cells that predicted shorter overall survival (OS) and relapse-free survival (RFS) in

105 breast cancer patients, reinforcing the clinical relevance of these findings.

106   Our results reveal a novel mechanism modulating tumor plasticity and triggering the

107   emergence of cancer cells with enhanced metastatic capacity, through paracrine (Tu-

108   Gr1+CD11b+-mediated) and cell autonomous (chemotherapy-induced) OSM/IL6-JAK

109   dependent signaling. The OSM/IL6-JAK axis may be considered as a candidate of

110   actionable clinical targets to impinge on metastatic progression and therapy resistance.

111

112   **Results**

113   **A Sca-1+ tumor cell population is enriched during tumor progression and has higher**

114   ***in vivo* metastatic capacity**

115   To investigate tumor cell heterogeneity during tumor progression, we first examined the

116   expression of the previously reported breast CSC markers CD24, CD44, CD61, Sca-1 and

117   CD49f (13) in the publicly available RNA sequencing (RNAseq) dataset from Ross *et al.*

118   encompassing several murine breast cancer models (37). This dataset includes data from

119   cultured cancer cells (In_Culture), orthotopic primary tumors (OT_PT), spontaneous lung

120   metastases (OT_LuM), and experimental lung metastases after tail vein injection

121   (TV_LuM) (Figure 1A and Supplemental Figure 1A). *Sca-1* expression was elevated in lung

122   metastasis in 4T1, 6DT1, Mvt1 and Met1 models compared with the respective primary

123   tumors. Interestingly, in 4T1, 6DT1 and Mvt1 models, *Sca-1* expression was also elevated

124   in experimental lung metastases compared with cultured cells. However, the expression of

125   *Cd24*, *Cd44*, *Cd61* and *Cd49f* were not altered, or their expression pattern was inconsistent

126   during progression (Supplemental Figure 1A). Thus, increased *Sca-1* expression during

127   metastasis is consistently observed in different preclinical breast cancer models.

128   To investigate whether the increased *Sca-1* expression within the tumor mass was

129   due to an increased gene expression in all cancer cells or to the enrichment of a Sca-1+

130   population, we orthotopically injected 4T1 tumor cells and determined the frequency of

131 different cell populations present in the primary tumor and lung metastases 30 days later

132 by flow cytometry (Figure 1B). We observed that the frequency of both Sca-1$^+$ and CD61$^+$

133 populations increased in lung metastases compared to primary tumors (Figure 1C). In

134 contrast, the CD24$^+$, CD44$^+$ and CD49f$^+$ populations were not significantly altered.

135   The enrichment of the Sca-1$^+$ population in lung metastases prompted us to ask

136 whether Sca-1$^+$ cells actively contribute to the metastasis. To this end, we isolated 4T1-

137 Sca-1$^+$ and 4T1-Sca-1$^-$ cells by magnetic activated cell sorting (MACS) from parental 4T1

138 cells, which contains low frequency of Sca-1$^+$ population (10-15%) (Supplemental Figure

139 1B, C), and examined their metastatic ability *in vivo*. In the orthotopic injection model, 4T1-

140 Sca-1$^+$ cells formed significantly more lung metastases than 4T1-Sca-1$^-$ cells, while there

141 was no significant difference in primary tumor growth (Figure 1D-F). Upon tail vein injection,

142 4T1-Sca-1$^+$ cells displayed significantly greater lung colonization ability compared to 4T1-

143 Sca-1$^-$ cells and a non-significant increase compared to parental 4T1 cells (Figure 1G-I).

144 In addition, 4T1-Sca-1$^+$ cells showed significantly higher *in vitro* mammosphere forming

145 efficiency than 4T1-Sca-1$^-$ cells (Supplemental Figure 2A), while *in vitro* cell growth and

146 cell motility were comparable (Supplemental Figure 2B-C).

147   These results suggest that 4T1-Sca-1$^+$ and 4T1-Sca-1$^-$ cells have similar tumorigenic

148 potential, while 4T1-Sca-1$^+$ cells have higher metastasis-initiating capacity.

149

150 **The Sca-1$^+$ tumor cell population is plastic *in vitro* and *in vivo***

151 Growing evidence indicates that cancer cells possess plastic features, which can be

152 modulated by both cell-intrinsic factors and microenvironmental cues (37, 38). To

153 characterize the observed plasticity of 4T1-Sca-1$^+$ cells, we first investigated isolated 4T1-

154 Sca-1$^+$ and 4T1-Sca-1$^-$ cells *in vitro*. The abundance of Sca-1$^+$ population in 4T1-Sca-1$^+$

155 cells enriched by MACS sorting (> 75%) gradually decreased to 50% after 4 days of culture

7

156   (Supplemental Figure 2D, upper panel), while the Sca-1$^-$ cells (negatively enriched by

157   MACS) regenerated a Sca-1$^+$ population (from less that 1% to 19%) (Supplemental Figure

158   2E, lower panel). Consistently, after orthotopic injection of 4T1-Sca-1$^+$ cells, the abundance

159   of the Sca-1$^+$ population in the derived tumors decreased from 75% to about 40% after 23

160   days of growth, while in tumors generated from 4T1-Sca-1$^-$ cells it increased from less than

161   1% to 15% (Supplemental Figure 2E), similar to the frequency of Sca-1$^+$ population in

162   tumors derived from parental 4T1 cells (Figure 1C). In addition, when tumor cells derived

163   from primary tumors and lung metastases of parental 4T1-injected mice were cultured *ex*

164   *vivo*, the abundance of the Sca-1$^+$ population significantly decreased from 20% to 4.5%

165   and 60% to 19%, respectively (Supplemental Figure 2F).

166   From these observations we conclude that both Sca-1$^+$ and Sca-1$^-$ populations are

167   highly plastic and this plasticity appears to be modulated *in vivo*.

168

169 Tumor-educated Gr1$^+$CD11b$^+$ cells expand the metastatic Sca-1$^+$ population

170   Immune cells in the TME are critical determinants of tumor cells functions and behaviors,

171   including metastatic capacity (39). To collect evidence for a potential correlation between

172   immune cells and the Sca-1$^+$ population, we characterized the inflammatory cells infiltrating

173   the orthotopic primary tumors. We observed a significant increase of the

174   Gr1^{high}CD11b$^+$Ly6C^{low} population and a significant decrease of the Gr1^{low}CD11b$^+$Ly6C^{high}

175   population in tumors derived from the 4T1-Sca-1$^+$ cells, compared to tumors derived from

176   the 4T1-Sca-1$^-$ cells (Figure 2A). Gr1^{high}CD11b$^+$Ly6C^{low} cells are immature myeloid

177   progenitors mobilized from the bone marrow by tumor-derived signals capable of

178   establishing an immunosuppressive environment facilitating tumor progression and

179   metastasis (40, 41). Gr1$^+$CD11b$^+$ cells form a homogenous population in the circulation

180   (Supplemental Figure 3A), consistent with the literature (42), while in the TME they

8

181 differentiated into two distinct subpopulations, Gr1^{high} and Gr1^{low}. To examine the direct

182 contribution of the tumor-educated Gr1$^+$CD11b$^+$ cells in promoting the enrichment of the

183 Sca-1$^+$ population, we isolated Gr1$^+$ cells from primary tumors, bone marrow and spleen of

184 4T1 tumor-bearing BALB/c mice by MACS, and co-cultured them *in vitro* with parental 4T1

185 cells (Figure 2B). Gr1$^+$ cells isolated from tumors (Tu-Gr1$^+$CD11b$^+$), but not from spleen

186 (Spl- Gr1$^+$CD11b$^+$) or bone marrow (BM-Gr1$^+$CD11b$^+$), significantly induced the expansion

187 of a Sca-1$^+$ population in 4T1 cells (from 12.5% to 81%, p<0.001) in 48 hours (Figure 2C).

188 To test whether the expansion of a Sca-1$^+$ population from 4T1 cells required direct contact

189 with Tu-Gr1$^+$CD11b$^+$ or was mediated by soluble factors, we compared the induction in two

190 different co-culture setups, either in standard wells (cell contact) or in Transwells, where

191 Tu-Gr1$^+$CD11b$^+$ and 4T1 cells were separated by a filter with 0.4 µm pores (Figure 2D).

192 We did not observe any significant difference in the induction efficiency of Sca-1$^+$

193 populations (measured by flow cytometry) between the two conditions and increasing the

194 4T1:Tu-Gr1$^+$CD11b$^+$ cell ratio from 1:1 to 1:3 did not further expand the Sca-1$^+$ population

195 (Figure 2E). Furthermore, conditioned medium from co-cultured Tu-Gr1$^+$CD11b$^+$ and 4T1

196 cells was also capable of subsequently expanding the Sca-1$^+$ population from 4T1 cells

197 alone (Supplemental Figure 3B). Interestingly, the Tu-Gr1$^+$CD11b$^+$ induced Sca-1$^+$

198 population appeared more stable in time compared to the isolated 4T1-Sca-1$^+$ cells

199 (Supplemental Figure 3C and Supplemental Figure 2E). More importantly, when

200 Gr1$^+$CD11b$^+$ cells-primed 4T1 cells were injected into the tail vein, Tu-Gr1$^+$CD11b$^+$ primed

201 ones showed higher lung colonization capacity compared to Spl-Gr1$^+$CD11b$^+$ primed one

202 (Figure 2F-H).

203   These results imply that tumor-educated Gr1$^+$CD11b$^+$ cells induce the emergence of

204 a highly metastatic Sca-1$^+$ population through secreted factors.

205

9

Tu-Gr1$^+$CD11b$^+$-induced and tumor-inherent Sca-1$^+$ populations display distinct gene expression profiles

To unravel the molecular basis for the metastatic capacity of the inherent 4T1- Sca-1$^+$ population and the Tu-Gr1$^+$CD11b$^+$ induced Sca-1$^+$ population, we first performed transcriptomic profiling of 4T1-Sca-1$^+$ and 4T1-Sca-1$^-$ cells isolated from the parental 4T1 line. Pathway enrichment analysis showed that 4T1-Sca-1$^+$ and 4T1-Sca-1$^-$ cells expressed different genes associated with distinct signaling pathways (Figure 3A). The top 200 significantly upregulated and downregulated genes were extracted as Sca1 Positive and Sca1 Negative signatures, respectively (Supplemental Table 1). Next, we performed transcriptomic profiling of Tu-Gr1$^+$CD11b$^+$-primed 4T1, Spl-Gr1$^+$CD11b$^+$-primed 4T1 and parental 4T1 cells. Pathway enrichment analysis revealed that Tu-Gr1$^+$CD11b$^+$ and Spl-Gr1$^+$CD11b$^+$ priming induced distinct transcriptomic alterations in 4T1 cells (Figure 3B). To focus on the transcriptomic alternations related to the Sca-1$^+$ population conversion, we compared Tu-Gr1$^+$CD11b$^+$-primed vs Spl-Gr1$^+$CD11b$^+$-primed cells. Interestingly, Tu-Gr1$^+$CD11b$^+$-primed 4T1 cells expressed both Sca-1 Positive and Sca-1 Negative signatures (Figure 3C), suggesting that Tu-Gr1$^+$CD11b$^+$ may twist tumor plasticity by converting the 4T1-Sca-1$^-$ cells into 4T1-Sca-1$^+$ cells, rather than expanding the pre-existing 4T1-Sca-1$^+$ population.

To test whether, despite the diverse transcriptional profiles across different Sca-1$^+$ populations, there could be a common molecular mechanism underlying their induction and metastatic capacity, we compared the significantly differentially expressed genes between 4T1-Sca-1$^+$ versus 4T1-Sca-1$^-$ and Tu-Gr1$^+$CD11b$^+$ primed 4T1 versus Spl-Gr1$^+$CD11b$^+$ primed 4T1 cells. Strikingly, among a total of 1118 up- and 423 down-regulated genes found when comparing the two conditions, only 56 up- and one down-regulated genes were shared (Figure 3D and Supplemental Table 1). This observation was

10

231   consistent with the notion that the Sca-1$^+$ population in Tu-Gr1$^+$CD11b$^+$ primed 4T1 cells

232   was different from the inherent 4T1-Sca-1$^+$ cells. Nonetheless, the fact that the 4T1-Sca-

233   1$^+$ cells and Tu-Gr1$^+$CD11b$^+$ primed 4T1 cells possessed similar *in vivo* metastatic capacity

234   suggested that among these common pathways some were relevant for 4T1 metastases

235   formation. To this end, we analyzed the publicly available scRNA-seq dataset from 4T1

236   primary tumors of Sebastian *et al.* (43). In this dataset, several cell types, including cancer

237   cells, epithelial cells, fibroblasts, distinct subpopulations of myeloid cells were identified

238   (43). To determine significant ligand-receptor interactions from the scRNA-seq data, we

239   performed cell-cell interaction analysis with CellPhoneDB (44) by focusing on the

240   interactions between epithelial/cancer cells and myeloid cells (Figure 3E, F). The analysis

241   identified 160 ligand-receptor interaction pairs (Supplemental Table 2). Among those pairs,

242   OSM receptor (OSMR) and pyrimidinergic receptor P2Y6 (P2RY6) were the only ones

243   present inside the 56 common genes shown in Figure 3D. However, P2RY6 interacts with

244   COPA (Coatomer Complex Subunit Alpha), a membrane protein involved in membrane

245   traffic between endoplasmic reticulum and Golgi (45) and, thus, unlikely to mediate cell-

246   cell contact-independent induction of the Sca-1$^+$ population. As the IL6-JAK-STAT3

247   signaling pathway was upregulated both in the 4T1-Sca-1$^+$ population and Tu-

248   Gr1$^+$CD11b$^+$-primed 4T1 cells (Figure 3A, B), we next examined the expression of *Osm*,

249   *Osmr*, *Il6st*, *Il6*, and *Il6* receptor (*Il6ra*) in the Sebastian dataset (Figure 3G). The

250   expression of *Il6* and *Osm* was restricted to myeloid cells, with *Osm* expression being more

251   prominent, similar to a previous report (33). *Osmr* was predominantly expressed in tumor

252   cells, while *Il6st* and *Il6ra* were homogenously expressed in all cell types.

253   We then explored their expression in the 4T1-Sca-1$^+$ cells and Tu-Gr1$^+$CD11b$^+$

254   primed 4T1 cells. *Osm* and *Il6* expression were very low in all samples (normalized count

255   number less than 7 on average) (Figure 3H-I), consistent with data in the Sebastian dataset

11

256 (Figure 3G). *Osmr* and *Il6ra*, however, were highly expressed in 4T1-Sca-1$^+$ cells

257 compared with 4T1-Sca-1$^-$ cells, while the expression of *Il6st* was abundant in both

258 populations, though higher in 4T1-Sca-1$^+$ cells (Figure 3H). On the other hand, only *Osmr*

259 was significantly upregulated in Tu-Gr1$^+$CD11b$^+$ primed 4T1 compared with Spl-

260 Gr1$^+$CD11b$^+$ primed 4T1 (Figure 3I).

261 Taken together, these results suggest that OSM/OMSR and IL6/IL6R signaling

262 pathways may be involved in the Tu-Gr1$^+$CD11b$^+$-mediated expansion of 4T1-Sca-1$^+$ cells.

263

264 **Tu-Gr1$^+$CD11b$^+$ cells promote Sca-1$^-$ to Sca-1$^+$ population conversion**

265 The above results strongly implied that Tu-Gr1$^+$CD11b$^+$ cells convert Sca-1$^-$ population into

266 the Sca-1$^+$ one. To further test this hypothesis, we compared the cell population dynamics

267 in cultured cells and the orthotopic primary tumors by analyzing publicly available scRNA-

268 seq datasets. By integrating scRNA-seq data from 3D cultured 4T1 cells (GSM4812003)

269 (46) and tumor cells isolated from orthotopically fat pad-injected 4T1 primary tumor (PT)

270 (GSM3502134) (47) (Figure 4A, B), we observed 5 clusters. Clusters 0, 1, 2, 4 were

271 predominant in cultured tumor cells, while cluster 3 was predominant in primary tumors.

272 Single-cell trajectories analysis confirmed that cluster 3 was at the end of the

273 transformation process (Figure 4C, D). The population dynamics also showed that the

274 fraction of cells in clusters 1, 2 and 4 decreased during the transformation, the one in

275 cluster 0 only minimally increased, while the fraction in cluster 3 massively increased

276 (Figure 4E). Importantly, very few cultured 4T1 cells expressed *Sca-1* while it was

277 abundantly expressed in the majority of cells in the primary tumor (Supplemental Figure

278 4A, upper panel). Consistently, the fraction of cells expressing *Osmr* was higher in the

279 primary tumor compared to cultured cells (Supplemental Figure 4A, lower panel). Similar

280 observations were obtained when analyzing scRNA-seq data from the ER$^+$ human breast

281 cancer model MCF-7. After integrating data from cultured MCF-7 cells (GSM4681765) and

282 tumor cells that were isolated from MCF-7 intraductal injected mammary gland

283 (GSM5904917) (48), 6 clusters were identified (Figure 4F), with clusters 1 and 3

284 predominant in cultured MCF-7 cells, while clusters 2 and 4 were predominant in primary

285 tumors (Figure 4G). Further analysis showed that clusters 2 and 4 expanded during *in vitro*

286 to *in vivo* tumor cell transformation and represented nearly 50% of the *in vivo* primary tumor

287 cells (Figure 4H-J). Although there is no human homolog of *Sca1* gene, *OSMR* expressing

288 cells were increased upon tumor implantation, especially in clusters 2 and 1 (Supplemental

289 Figure 4B).

290 To further investigate the signals involved in this transformation, we performed

291 GSAE analysis for cluster 3 in 4T1 cells and clusters 2 and 4 in MCF-7 cells, respectively

292 (Figure 4K-N). By comparing the Hallmark gene signatures, IL6-JAK-STAT3 signature was

293 significantly upregulated in both cell populations (Figure 4K, M). Interestingly, Sca1

294 Positive and Sca1 Negative signatures were both upregulated (Figure 4L, N), which is

295 consistent with our *ex vivo* induction experiment (Figure 3C). To validate the involvement

296 of Tu-Gr1$^+$CD11b$^+$ during the cell population transformation, we extracted the top 50

297 upregulated genes (Supplemental Table 3) identified by comparing the Tu-Gr1$^+$CD11b$^+$

298 with the Sp-Gr1$^+$CD11b$^+$-stimulated 4T1 cells as Tu-Gr1$^+$CD11b$^+$ induced signature. Both

299 cell populations predominant in the primary tumor in both 4T1 and MCF-7 models,

300 upregulated the Tu-Gr1$^+$CD11b$^+$ induced signature (Figure 4L, N).

301 These data, together with our *in vivo* observations (Figure 1A-C) and *ex vivo*

302 coculture experiments (Figure 2B-E and Figure 3C), indicate that Tu-Gr1$^+$CD11b$^+$ convert

303 the Sca-1$^-$ population to Sca-1$^+$ population, likely, via OSM/IL6 signaling pathway.

304

13

OSM/IL6-JAK pathway mediates Tu-Gr1$^+$CD11b$^+$-induced Sca-1$^+$ population enrichment

To experimentally interrogate the role of OSM/IL6 in modulating the Sca-1$^+$ population, we first measured *Osm* and *Il6* mRNA expression in Spl-Gr1$^+$CD11b$^+$ and Tu-Gr1$^+$CD11b$^+$. Indeed, both *Osm* and *Il6* mRNA levels were significantly elevated in Tu-Gr1$^+$CD11b$^+$ (Figure 5A). To functionally validate the role of OSM/IL6 in the generation of Sca-1$^+$ population, we treated 4T1 cells directly with recombinant OSM and IL6 proteins *in vitro* and measured the effect on the Sca-1$^+$ population. After 2 days of treatment, both OSM and IL6 significantly increased the frequency of Sca-1$^+$ cells from 16% to 38.8% and 26.5%, respectively (Figure 5B). Conversely, blocking OSM and IL6 activities using anti- OSM or -IL6 neutralizing antibodies significantly reduced the emergence of Sca-1$^+$ population induced by Tu-Gr1$^+$CD11b$^+$ conditioned medium (Figure 5C). The combination of anti-OSM and -IL6 antibodies did not have additive effects suggesting that OSM and IL6 both contribute in promoting Sca-1$^+$ population by sharing the same signaling cascades.

OSMR and IL6R signal by activating the intracellular Janus tyrosine kinase (JAK) (49). To explore the involvement of the JAK pathway in the emergence of the Sca-1$^+$ population, we treated 4T1 cells with the JAK inhibitor (Ruxolitinib) during exposure to recombinant OSM and IL6. Ruxolitinib treatment prevented the emergence of the Sca-1$^+$ population in response to recombinant OSM and IL6 (Figure 5D).

From these results, we conclude that OSM/IL6-JAK pathway mediates Tu-Gr1$^+$CD11b$^+$ -induced Sca-1$^+$ population enrichment.

Tu-Gr1$^+$CD11b$^+$-induced Sca-1$^+$ population and 4T1-inherent Sca-1$^+$ population have distinct CSC and EMT gene expression profiles

329   OSM/IL6-JAK signaling has been reported to support tumor progression by promoting a

330   CSC phenotype and epithelial-mesenchymal plasticity (25, 36, 50). To further characterize

331   CSC and EMT features in 4T1-Sca-1$^+$ cells and Tu-Gr1$^+$CD11b$^+$ induced Sca-1$^+$

332   population, we interrogated our RNAseq data set for the expression of 17 stem cell and

333   EMT markers (Supplemental Figure 5). The stem cell markers *Oct4* (*Pou5f1*), *Sox2* and

334   *Nanog* were undetectable or very low in all or some samples. 4T1-Sca-1$^+$ cells had higher

335   expression of *Aldh1a1*, *Aldh3a1* and *Podxl* but lower expression of *Klf4* and *Sox9*

336   compared to 4T1-Sca-1$^-$ cells. There was no difference in the expression of *Abcg2* and

337   *Has2*. Tu-Gr1$^+$CD11b$^+$ primed 4T1 cells had higher expression of *Klf4* and *Has2*, lower

338   expression of *Aldh1a1*, *Aldh3a1* and *Sox9*, and similar expression of *Podxl* when

339   compared with Spl-Gr1$^+$CD11b$^+$ primed 4T1. Among them, only *Has2* expression was

340   specifically elevated in Tu-Gr1$^+$CD11b$^+$ primed 4T1 compared with control 4T1 and Spl-

341   Gr1$^+$CD11b$^+$-primed 4T1 (Supplemental Figure 5A). On the other hand, 4T1-Sca-1$^+$ cells

342   had lower expression of *Cdh1* and higher expression of *Snail1*, *Twist1*, *Vim* and *Foxc1*

343   which support an EMT status, although *Zeb1* expression was reduced (Supplemental

344   Figure 5B). Globally, the expression of most of the EMT genes were similar between Tu-

345   Gr1$^+$CD11b$^+$ and Spl-Gr1$^+$CD11b$^+$ primed 4T1 cells, except for *Snail2* and *Vim*, whose

346   expression was suppressed in Tu-Gr1$^+$CD11b$^+$ primed 4T1 (Supplemental Figure 5B).

347   Taken together, these results indicate that the Tu-Gr1$^+$CD11b$^+$-induced Sca-1$^+$

348   population and inherent Sca-1$^+$ population have different CSC and EMT transcriptional

349   profiles, reinforcing the notion that, Tu-Gr1$^+$CD11b$^+$-induced Sca-1$^+$ population are not just

350   enriched tumor-inherent Sca-1$^+$ population

351

352   **Chemotherapy enriches a Sca-1$^+$ population with CSC features**

353 CSC and cancer cell plasticity contribute to drug resistance in various tumor types,

354 including breast cancer (51–55). The above results, including the significantly elevated

355 expression of *Aldh3a1* (a marker of drug resistance) in the 4T1-Sca-1$^+$ population

356 prompted us to investigate the resistance of this population to chemotherapy. To this end,

357 we treated 4T1 cells for 48 hours *in vitro* with methotrexate (MTX) and doxorubicin (Dox),

358 two widely used chemotherapy drugs, including in breast cancer. The 48 hours treatment

359 of either drug increased the frequency of Sca-1$^+$ population in 4T1 cells (Figure 6A). Next,

360 we mimicked a clinically relevant situation of cancer cells escaping chemotherapy by

361 exposing 4T1 cells to 28 nM MTX, a concentration slightly higher than the IC$_{50}$

362 concentration of the drug, for up to 3 weeks and recovered the surviving cells by switching

363 to normal medium (Figure 6B). The selected cell line, named MR13, was highly enriched

364 in Sca-1$^+$ cells (>60%) (Figure 6C). Compared to parental 4T1 tumor cells, MR13 cells

365 exhibited a higher mammosphere forming efficiency (Figure 6D), lower *in vitro* proliferative

366 capacity (Figure 6E) and increased cell mobility (Figure 6F), which were consistent with

367 CSC-like properties. When tested in a 48-hours cytotoxicity assay, MR13 cells were more

368 resistant against MTX compared to parental 4T1 (Supplemental Figure 6A).

369

370 **MR13-derived tumors are highly metastatic and rich in Gr1^{high}CD11b$^+$ Ly6C^{low} cells**

371 To characterize the *in vivo* behavior of MR13 cells, we orthotopically implanted them into

372 BALB/c mice and monitored the progression. MR13 cells formed smaller primary tumors

373 relative to parental 4T1 cells, that were more metastatic to the lung (Figure 6G-I) and

374 enriched in Gr1^{high}CD11b$^+$ Ly6C^{low} cells compared to 4T1 tumors (Figure 6J), similarly to

375 4T1-Sca-1$^+$-derived tumors (Figure 2A). Strikingly, we observed metastases in the heart

376 (Supplemental Figure 6B), which we never observed with the parental 4T1 cells. MR13

377 cells retained a large fraction of the Sca-1$^+$ population *in vitro*, even when cultured in the

378   absence of MTX (Figure 6C) and upon *in vivo* expansion (Figure 6K). Such stability of Sca-

379   1 population contrasted with 4T1-Sca-1$^+$ cells and Tu-Gr1$^+$CD11b$^+$-primed 4T1 cells

380   (Supplemental Figure 2E, G) that, upon isolation or induction reverted to a Sca-1$^-$

381   phenotype, suggesting that MR13 line was capable of self-sustain its own Sca-1$^+$

382   population.

383   Taken together, chemotherapy-selected MR13 cells share some similar *in vivo*

384   characteristics as 4T1-Sca-1$^+$ cells, while they are capable of self-sustaining high Sca-1$^+$

385   abundancy both *in vitro* and *in vivo.*

386

387   **IL6/IL6R-JAK autocrine signaling maintains Sca-1 positivity and metastatic capacity**

388   **in MR13 cells**

389   To better understand the chemotherapy-induced alterations in MR13 cells, we performed

390   transcriptomic analyses comparing MR13 and parental 4T1 cells. Pathway enrichment

391   analysis showed that the IL6-JAK-STAT3 signature was also elevated in MR13 cells

392   (Figure 7A). Importantly, MR13 gene expression significantly positively correlated with the

393   Sca1 Positive signature. At the same time, it negatively correlated with the Sca1 Negative

394   signature (Figure 7B). This observation suggested that chemotherapy enriched for the

395   inherent 4T1-Sca-1$^+$ population, rather than converting plastic Sca-1$^-$ cells, as observed

396   upon Tu-Gr1$^+$CD11b$^+$-stimulation. In addition, *Osmr*, *Il6*, *Il6ra* and *Il6st* were all

397   overexpressed in MR13 cells compared to parental 4T1 cells, while the *Osm* expression

398   was not altered (Figure 7C). To functionally validate the IL6-JAK signaling pathway in Sca-

399   1$^+$ population maintenance, we treated MR13 cells with Ruxolitinib *in vitro* for 48 hours*.*

400   The treatment significantly decreased the fraction of Sca-1$^+$ cells (Figure 7D). Importantly,

401   *in vitro* treatment of MR13 cells with Ruxolitinib for 3 days nearly completely abolished their

402   lung metastatic capacity upon tail vein injection (Figure 7E-F).

403   Altogether, these data suggest that MR13 cells sustain the metastatic Sca-1+

404   population through cell-autonomous activation of the IL6-JAK signaling pathway.

405

406   **Tu-Gr1+CD11b+ invoked tumor cell signature predicts shorter overall and relapse-**

407   **free survival in breast cancer patients**

408   To evaluate the clinical relevance of the crosstalk between Tu-Gr1+CD11b+ and tumor

409   cells, we tested whether the Tu-Gr1+CD11b+-induced 4T1 signature could predict cancer

410   progression in patients. To this end, we interrogated the METABRIC dataset (56) with the

411   Tu-Gr1+CD11b+-induced signature. Thirty-two human orthologue genes (Supplemental

412   Table 3) in the murine 50 genes signature were present in the METABRIC dataset. Patients

413   with the higher expression level of the signature had shorter overall survival (OS; p =

414   0.0056) and relapse-free survival (RFS; p = 0.032) (Figure 8A, B). Notably, OSM

415   expression positively correlated with the signature in all patients (Supplemental Figure 7A),

416   suggesting OSM do contribute to altered signature expression in patients. Of the thirty-two

417   genes, five (*MX1, IRF7, OAS1, CMPK2, ISG15*) were commonly discriminant for a shorter

418   OS and RFS (Figure 8C, D), and taken together, they further enhanced the predictive

419   power (OS: p=0.00055; RFS: p=0.00069) (Figure 8E, F).

420   These data indicate that a small set of genes issued from the murine tumor cell

421   signature invoked by Tu-Gr1+CD11b+ cells can predict a shorter OS and RFS in breast

422   cancer patients, thereby reinforcing the clinical significance of the proposed model.

423

424   **Discussion**

425   Metastatic disease and therapy resistance are the leading causes of breast cancer

426   mortality, calling for novel approaches to effectively prevent and cure for metastasis and

427   therapy resistance. This is particularly relevant for TNBC, where in spite of the recent

18

428 encouraging results with targeted therapies, such as PARP inhibitors for tumors with

429 germline BRCA mutations, or checkpoint inhibitors for PD-L1[+] tumors, management of

430 metastatic disease remains challenging (57–60). It has been proposed that CSCs present

431 in the primary tumor are responsible for tumor persistence, metastasis, and therapy

432 resistance (52, 61). Enrichment and differentiation of CSC contribute to tumor

433 heterogeneity (17, 19–22). Importantly, CSC features can be intrinsic or plastic and be

434 modulated by cues from the TME (62–64).

435 Here, we have interrogated the contribution of the Sca-1^{+} population to breast

436 cancer metastasis and its modulation by the TME. We reported that tumor-educated

437 Gr1^{+}CD11b^{+} cells (Tu-Gr1^{+}CD11b^{+}) instigate cancer metastasis by twisting cancer cell

438 plasticity and enriching for a Sca-1^{+} population with enhanced metastatic capacity. We

439 identified OSM/IL6-JAK as a paracrine communication axis between Tu-Gr1^{+}CD11b^{+} and

440 breast cancer cells and as an autocrine loop in chemotherapy-resistant tumor cells,

441 promoting tumor heterogeneity, CSC features and metastatic capacity. Importantly, breast

442 cancer patients expressing high levels of the human orthologues of the gene expression

443 signatures invoked by Tu-Gr1^{+}CD11b^{+} have significantly shorter OS and RFS, reinforcing

444 the clinical significance of our findings. While some of these elements have been reported

445 individually before, our results extend these observations by providing an integrative view

446 of paracrine (Tu-Gr1^{+}CD11b^{+}-induced) and autocrine (chemotherapy-induced)

447 communication in regulating tumor heterogeneity, cancer cell plasticity, metastasis, and

448 resistance to chemotherapy.

449 A main observation stemming from this study is that Sca-1^{+} population exists under

450 three different conditions: as inherent 4T1-Sca-1^{+} population, upon exposure to Tu-

451 Gr1^{+}CD11b^{+} cells and upon chemotherapy treatment (MR13). All these populations had

452 higher metastatic abilities compared to their counterpart controls. GSEA analysis

453   suggested that the Tu-Gr1$^+$CD11b$^+$-induced Sca-1$^+$ population was likely to convert from

454   the Sca-1$^-$ population (Figure 3C and Figure 4), while the Sca-1$^+$ population surviving

455   chemotherapy (MR13) appeared to be enriched from the inherent Sca-1$^+$ population

456   (Figure 7B). In addition, the different gene expression signature of Tu-Gr1$^+$CD11b$^+$-

457   induced Sca-1$^+$ population relative to the inherent Sca-1$^+$ cells suggest a remarkable

458   functional plasticity of these cells. This plasticity is further supported by comparing single

459   cell gene expression of murine 4T1 and human MCF-7 breast cancer cells, using publicly

460   available scRNA-seq datasets, before and after *in vivo* growth (Figure 4). *In vivo*, tumor

461   cells undergo a transformation enriching for Sca-1 (in the mouse), OSMR expressing cells,

462   Sca1 Positive, Sca1 Negative and Tu-Gr1$^+$CD11b$^+$-induced signatures, and IL6-JAK

463   signaling pathway from precursor cells (Sca-1$^-$ in the mouse) (Figure 4). Gong *et al.* have

464   reported that sorted Sca-1$^-$ 4T1 cells could be transiently transformed into a Sca-1$^+$

465   population by radiotherapy (65). An analogous observation was reported in colorectal

466   cancer, where selective ablation of LGR5$^+$ CSCs in organoids leads to initial tumor

467   regression, followed by regrowth driven by LGR5$^+$ CSCs reemerging from the LGR5$^-$

468   population (66). Taken together, by demonstrating that tumor recruited and educated

469   Gr1$^+$CD11b$^+$ cells contribute to such plasticity by inducing the conversion of low metastatic

470   Sca-1- population into a highly metastatic Sca-1$^+$ population, our observations further

471   consolidate the notion that cancer consists of a heterogenous and plastic tumor mass,

472   including highly metastatic cell populations. Dedicated time course scRNA-seq analyses

473   together with lineage tracing experiments may help to further characterize the detailed

474   origin, development, fate, and function of these Sca-1$^+$ populations during cancer

475   progression.

476   Recruitment and accumulation of Gr1$^+$CD11b$^+$ cells in the TME, particularly through

477   the chemokines CCL2, CXCL1 and CXCL2, or IL-33, is considered a critical step for their

478   contribution to tumor progression and metastasis (67–70). Consistent with these

479   observations, tumors derived from sorted 4T1-Sca-1$^+$ cells, or MR13 cells that are

480   intrinsically enriched for Sca-1$^+$ cells, have a higher content of Gr1^{high}CD11b$^+$Ly6C^{low} cells

481   compared to tumors derived from 4T1-Sca-1$^-$ or parental 4T1 cells, respectively (Figure 2A

482   and 5K). Beyond recruitment, tumor-mediated education of Gr1$^+$CD11b$^+$ cells, appears to

483   be necessary to gain higher metastatic activity: Only Gr1$^+$CD11b$^+$ cells recovered from

484   primary tumors (but not from spleen or bone marrow) induced Sca-1 positivity and

485   enhanced metastatic ability in 4T1 cells (Figure 2C, E). The role of Gr1$^+$CD11b$^+$ cells in

486   promoting metastasis has been mainly attributed to promotion of angiogenesis, EMT and

487   immunosuppression (17, 68). Peng *et al.*, reported the ability of those cells to endow CSC-

488   like features to breast cancer cells but their metastatic capacity was not interrogated (17).

489   Our observations suggest a self-sustaining positive feedback mechanism between highly

490   metastatic cancer cells (Sca-1$^+$ population) and Gr1$^+$CD11b$^+$ cells: inherent Sca1$^+$ CSC-

491   like, metastatic, cells promote recruitment and local education of Gr1$^+$CD11b$^+$ cells, which

492   in turn promote tumor heterogeneity, cancer cell plasticity and metastatic capacity by

493   converting low-metastatic Sca1$^-$ cells into additional high-metastatic Sca1$^+$ cells (Figure 9).

494   Recently, it was reported that neutrophils escorting blood circulating tumor cells (CTCs)

495   expands the metastatic potential of CTCs (71). While this effect was attributed to the

496   promotion of cell cycle progression of CTCs through direct contact with the neutrophils, in

497   light of our findings, one may also consider the possibility that clustered neutrophils may

498   also promote the expansion of a CSCs-like phenotype with higher metastatic capacity.

499   Interestingly, OSM was reported to be expressed by neutrophils cocultured with breast

500   cancer cells (36) and to promote phenotypic changes associated with mesenchymal and

501   stem cell-like differentiation in breast cancer (36, 72). Together with our observation, these

502   findings further reinforce the notion that boosting the *Osm* expression in Gr1$^+$CD11b$^+$ cells

21

503   is part of their educating program prompted by the tumor. One outstanding question raised

504   by these observations is by which mechanisms and pathways cancer cells, in particular

505   Sca-1+ ones, educate Gr1+CD11b+ cells to acquire cancer plasticity-promoting activity.

506   Besides directly activating tumor cells, OSM has also been shown to remodel

507   macrophages and fibroblasts of the TME (33, 36). Araujo *et al.* recently reported that OSM

508   derived from tumor-infiltrating myeloid cells reprogram fibroblasts to secrete VEGF and the

509   chemokines CXCL1 and CXCL16, resulting in enhanced myeloid cell recruitment and

510   breast cancer progression (33). Here we extend these observations by demonstrating that

511   tumor-educated Gr1+CD11b+-derived OSM/IL6 twist cancer cell plasticity by promoting a

512   rapid but reversible conversion of Sca-1- cells into more metastatic Sca-1+ cells (Figure

513   5B). We further broaden the implications of the OSM/IL6-JAK axis, by demonstrating that

514   MR13 cells that have escaped chemotherapy hijacked this paracrine mechanism in a cell

515   autonomous manner by elevating the *Il6* expression (Figure 9). Significantly, a short *in vitro*

516   treatment with Ruxolitinib effectively abrogated their metastatic capacity (Figure 7E, F).

517   While OSM/OSMR is the only interaction pair identified by the cell-cell interaction

518   analysis (Figure 3F, G), it is possible that other molecular mechanisms may also play roles

519   in modulating Sca-1+ cell plasticity and metastasis. One candidate is the IL6/IL6R

520   communication axis, which was less prominent in the cell-cell communication analysis

521   (Figure 3F, G), but highly expressed in our experimental data in Tu-Gr1+CD11b+ compared

522   with Spl-Gr1+CD11b+ (Figure 5A) and in chemotherapy-resistant MR13 cells compared

523   with 4T1 (Figure 7C). Moreover, the neutralization of IL6 also suppressed the Tu-

524   Gr1+CD11b+ conditioned medium induced Sca-1+ cell enrichment, much alike OSM

525   inhibition (Figure 5C).

526   Importantly, we demonstrated that a human orthologue signature of the 4T1 gene

527   expression signature invoked by Tu-Gr1+CD11b+ can predict a significantly shorter OS and

528   RFS in breast cancer patients (Figure 8). This finding strengthens the clinical significance

529   of the observed crosstalk between Tu-Gr1$^+$CD11b$^+$ and tumor cells. Strikingly, the five

530   genes that significantly contribute to the discriminatory power of the signature are genes

531   related to native or viral immunity or regulated by interferon. While expression of interferons

532   and interferon response genes in breast cancer has been mainly associated with tumor

533   suppression and improved survival (73), there is evidence also correlating interferon

534   responses with tumor promotion, therapy resistance and reduced survival (74). As

535   JAKs/STATS are activated by both IFN and OSM/IL6 receptors, it is conceivable that

536   OSM/IL6 only activates a subset of the IFN-induced genes with tumor-promoting activity,

537   as the case for Mx1 (75). Consistent with our findings, JAK/STAT signaling has recently

538   been shown to initiate the lineage plasticity in prostate cancer as well as to promote lineage

539   plasticity-driven targeted therapy resistance in a stem-like subpopulation of prostate cancer

540   (76, 77). On the other hand, Aouad *et al.* showed that epithelial-mesenchymal plasticity is

541   essential for the generation of a dormant cell state of ER$^+$ breast cancer during progression,

542   and the activation of IL6-JAK-STAT signaling triggers tumor cell awakening and recurrence

543   (48).

544   One crucial question raised by these results is whether the OSM/IL6-JAK pathway is

545   a potential actionable clinical target to impinge on metastatic progression and therapy

546   resistance. In particular, the observation that a short *in vitro* treatment of the highly

547   metastatic MR13 cells profoundly suppressed their metastatic capacity *in vivo* (Figure 7E,

548   F), suggests potential long-lasting effects consistent with an adjuvant effect. JAK inhibitors

549   are being tested in clinical trials in breast cancer. A phase I study combining Ruxolitinib

550   with paclitaxel in HER2-negative metastatic breast cancer showed good tolerability and

551   evidence of activity (78). A phase I/II trial of Ruxolitinib in combination with trastuzumab in

552   metastatic HER2 positive breast cancer and a phase II study combining Ruxolitinib with

23

553 capecitabine in advanced HER2- breast cancer, however, did not improve progression-free

554 survival (79, 80). The absence of benefits in these studies in advanced breast cancer and

555 our reported mechanistic observations on metastatic progression, raise the question of

556 whether the JAK inhibitors should be considered in adjuvant setting in high-risk patients,

557 to prevent progression to metastases, rather than treating patients already bearing

558 metastases.

559 In conclusion, we reported here that a subpopulation of tumor cells within the tumor

560 mass educates requited Gr1+CD11b+ cells to convert a low metastatic subpopulation into

561 highly metastatic one, through the OSM/IL6-JAK signaling axis (Figure 9). The clinical

562 relevance of this observation is supported by human transcriptomic data. This process is

563 hijacked by tumor cells that survived chemotherapy and evolved toward a highly metastatic

564 phenotype via cell autonomous IL6-JAK signaling. Importantly, a short *in vitro* treatment

565 with a clinically approved JAK inhibitor, Ruxolitinib, suppresses their metastatic capacity

566 these cells *in vivo.* These results should stimulate considering testing JAK inhibitors in the

567 adjuvant setting in TNBC breast cancer patients at high-risk for metastatic progression.

568

569

570 **Methods**

571 **Cell culture.** The 4T1 murine breast cancer cell line was kindly provided by Dr Fred R.

572 Miller (Michigan Cancer Foundation, Detroit, MI, USA). 4T1 cells were cultured in high

573 glucose DMEM supplemented with 10% heat-inactivated FBS, 1% penicillin–streptomycin

574 (P/S, from Gibco) and 1% Non-Essential Amino Acid (Gibco).

575

576 **Tumor models.** 4T1, MR13, sorted 4T1-Sca-1+ and 4T1-Sca-1- (5×10^4 cells in 50µl

577 PBS/10% of 8.1 mg/ml Matrigel Matrix, were injected in the fourth right mammary gland of

578 mice. Prior to surgery, ketamine (1.5 mg/kg) and xylazine (150 mg/kg) (both from Graeub)

579 were injected intra-peritoneally to anesthetize the animals. Immune cell populations were

580 analyzed at different time points post-tumor cell injection. Tumor length and width were

581 measured twice a week with caliper and used to calculate tumor volume by the following

582 equation: volume = (length x width^2) x π/6. Tumors were collected and weighted at

583 necropsy. For the intravenous injections, $2x10^5$ sorted 4T1-Sca-1$^+$ and 4T1- Sca-1$^-$ tumor

584 cells resuspended in a volume of 50 µl of PBS were injected into the mice tail vein. Lung

585 metastases were quantified 10 days post-injection. At each indicated time point, mice were

586 sacrificed according to defined ethical criteria and were killed by CO_2 inhalation followed

587 by neck dislocation or terminal bleeding. All animal procedures were performed in

588 accordance with the Swiss legislations on animal experimentation and approved by the

589 Cantonal Veterinary Service of the Cantons Vaud and Fribourg for experiments in

590 Lausanne and Fribourg (VD_1486.2; 2017_34_FR; 2017_34_FR, 2014_58_FR; 2011-33-

591 FR).

592

593 **Reagents and chemicals.** Growth factor reduced Matrigel Matrix (MG) was obtained from

594 Becton Dickinson (BD Biosciences). Collagenase I was purchased from Worthington and

595 DNAse I from Roche. Bovine serum albumin (BSA), crystal violet (CV) and

596 paraformaldehyde (PFA) were obtained from Sigma-Aldrich. Drugs, inhibitors and

597 cytokines: Doxorubicin and Methotrexate (generously provided by the Department of

598 Oncology, University Hospital, University of Lausanne, Lausanne, Switzerland), Ruxolitinib

599 (JAK inhibitor, Cat N°7064, Biotechne), anti-mouse Oncostatin M (R&D systems), anti-

600 mouse IL-6 (BioxCell), recombinant mouse Oncostatin M and IL-6 (Biolegend, Cat #:

601 762802 & 575702 respectively).

602

Antibodies. The following anti-mouse antibodies were used following manufacturer's instructions: anti-CD16/CD32 Fc blocking antibody (BD Biosciences), anti-CD24-FITC (clone M1/69, eBioscience), anti-CD29-PE and-PE-Cy5 (clone HMβ1-1, BioLegend), anti-Sca-1-APC (clone D7, eBioscience), anti-CD61-Alexa 647 (clone 2C9.62(HMβ3-1), BioLegend, anti-CD45-PE (clone 30-F11, BD Biosciences), anti-Gr1-eFlour450 (clone RB6-8C5,eBioscience), anti-Ly6C FITC (clone HK1.4, BioLegend), anti-Ly6G-APC (clone 1A8-Ly6g,eBioscience), anti-F4/80 PerCP/Cy5 (clone BM8, eBioscience), anti-CD11b-PE-Cy7 (clone M1/70,eBioscience), anti-CD11c-APC-eFluor780 (clone N418, eBioscience), anti-CD4-FITC (clone 6K1.5, eBioscience), anti-CD8-PE (clone 53-6.7, eBioscience), anti-B220-APC (clone RA3-6B2, eBioscience), anti-CD49b-eFlour450 (clone DX5, BioLegend), Annexin V-APC (clone B217656, BioLegend), Propidium Iodide-PerCP (Clone V13245, Life technologies).

Magnetic cell sorting (MACS). MACS separators were used for positive and negative cell selections based on manufacturer's instructions. Briefly, cells were counted and resuspend in 500 µl of MACS buffer with 10 µl of fluorescent coupled antibody of interest (APC-conjugated anti-Sca-1 and PE-conjugated anti-Gr1) per 10^7 cells added. Cells were incubated for 30 minutes in the dark at 4°C and then washed with MACS buffer. After centrifugation and resuspension in 80 µl of MACS buffer per 10^7 cells, 20 µl of anti- APC-conjugated magnetic beads (Miltenyi Biotec) per 10^7 cells was added. After a 20 minutes incubation in the dark at 4°C, cells were washed with MACS buffer. After the centrifugation they were resuspended in MACS buffer and the magnetic separation was performed using LS MACS column (maximum 10^8 labeled cells) for positive selection and LD MACS column (maximum 10^8 labeled cells) for negative selection (Miltenyi Biotec). The purity of positive subpopulation was >70% and <99% for the negative subpopulation.

628

Co-culture of Gr1+CD11b+ cells sorted from tumors or spleen of 4T1 tumor bearing mice. Gr1+ cells were sorted from tumors or spleen at day 23 post-injection (see below Magnetic beads cell sorting section). Afterwards, 1.5×10^5 4T1 cells were co-cultured in 6 wells plates using Transwell plates (0.4 μm, Nunc, ThermoFisher Scientific) with Gr1+CD11b+ sorted cells (top) and 4T1 cells (bottom) at different 4T1: Gr1+CD11b+ ratios (1:1, 1:3 and 1:5). After 48 hours of co-culture, cells were analyzed for Sca-1 expression and gene expression by flow cytometry and semi-quantitative real-time qPCR as indicated.

636

Flow cytometry analysis on tissue samples. Mice were sacrificed at different time points for blood and tumors collection. Tumors were cut in small pieces with scissors, washed, and digested in serum free medium supplemented with Collagenase I and DNAse I (Roche). The mixture was incubated at 37 °C for 45 minutes on a shaking platform. Subsequently, serum-supplemented medium was added to neutralize the enzymatic reaction and the tissue suspensions were filtered through a 100 μm and a 70 μm sterile nylon gauzes. Upon centrifugation (5 minutes at 1400 rpm), pellets were recovered and red blood cells lysed with ACK buffer (Biolegend). The staining procedure and the flow cytometry acquisition are as described previously (81). Data acquisition was performed using the FACSCalibur (BD Biosciences) or MACSQuant flow cytometer from Miltenyi Biotec and data analyzed by FlowJo v10.0.7 (tree Stat Inc.).

648

In vitro **cell proliferation assay**. Cells were collected and seeded in tissue culture 96-wells-plates (Costar) at 3'000 cells/well. Cells were grown in complete medium for 24, 36, 72 and 96 hours. At each time point cells were washed once with PBS, then fixed with 4% PFA and stained with 0.5% crystal violet solution for 0.5 hours. The stained cells were

653   gently washed with deionized water to remove the extra dye and air-dried overnight at

654   room temperature. After solubilizing the dye with crystal violet eluting buffer (70% ethanol

655   and 1% acetic acid), cell viability was assessed by reading the absorbance at 595 nm

656   wavelength in a multiwell plate reader (Modulus II microplate reader, Turner Biosystems).

657   Results were analyzed by Prism (Graph pad software, Inc.) expressed as mean values of

658   optical density (OD) of octuplet determinations ± SEM.

659

660   ***In vitro* cytotoxic assay.** Tumor cells were plated at a concentration of 3'000 cell/well into

661   96-wells plates. The following day, a series of concentrations of the different drugs were

662   supplemented to the culture medium. Untreated control cells were kept in normal culture

663   medium. Cell viability of each well was assessed with crystal violet staining 48 hours after

664   treatment, as described above. Results were analyzed by Prism software by a non-linear

665   regression analysis and expressed as relative cell viability compared with non-treated

666   control. The 50% maximum inhibition concentrations (IC_{50}) were used to determine the

667   drug-resistant ability of treated cells.

668

669   **Real-time reverse transcription qPCR and primers.** Changes in mRNA expression

670   levels were determined by semi-quantitative real-time qPCR. RNA samples were obtained

671   from adherent cells using RNeasy kit from QIAGEN according to manufacturer's

672   instructions. From each sample, 1 µg RNA was retro-transcribed using SuperScript II

673   Reverse Transcriptase kit (Life Technologies – Invitrogen), according to manufacturer's

674   instructions. The reactions were performed in a StepOnePlus™ thermocycler (Applied

675   Biosystems, Life Technologies – Invitrogen) using the KapaSYBR® FAST SYBR Green

676   Master Mix (Kapa Biosystems). Each reaction was performed in triplicates and values were

677   normalized to murine 36B4 housekeeping gene. The comparative C_t method was used to

678 calculate the difference of gene expression between samples. The following murine-

679 specific primers (Microsynth AG) were used:

680 Sca-1 (F:5'-TCAGGAGGCAGCAGTTATTGTG-3',R: 5'-TGGCAACAGGAAGTCTTCACG-

681 3'), 36B4(F:5'-GTGTGTCTGCAGATCGGGTAC-3',R:5'-CAGATGGATCAGCCAGGAAG-

682 3'), OSM (F: 5'- ATGCAGACACGGCTTCTAAGA-3', R: 5'- TTGGAGCAGCCACGATTG

683 G-3'), OSMR: (F: 5'- CATCCCGAAGCGAAGTCTTGG-3', R: 5'-

684 GGCTGGGACAGTCCATTC TAAA-3'), IL-6: (F: 5'- TACCACTTCACAAGTCGGAGGC-3',

685 R: 5'- CTGCAAGTGCATCAT CGTTGTTC-3').

686

687 **Histopathology.** Tumors and lungs were harvested at the end of the experiments, fixed in

688 formalin and embedded in paraffin. 5 µm thick serial sections were cut from the tissue

689 blocks. 3-4 sections taken at 100 µm distance were stained with hematoxylin and eosin

690 (H&E) and used to assess tumor morphology and quantify lung metastasis. Slides were

691 scanned by Nanozoomer (Hamamatsu Photonics) and metastasis were counted manually

692 using NDP.viewer2 software (Hamamatsu Photonics). Metastatic index was calculated by

693 normalizing the metastasis number with the volume of primary tumor.

694

695 **Mammosphere-forming assay** 5'000 cells/well were seeded in non-adhesive U bottom

696 96-wells plate in a semi-solid MEGM medium supplemented with 20 ng/ml EGF, and 20

697 ng/ml bFGF and heparin. Medium was gently replaced every 3 to 4 days. After 11 to 14

698 days culture, mammospheres of 50 to 150 µm diameter were detected under the

699 microscope (bright field) and counted to quantify the sphere formation efficiency (SFE) as

700 percentage of the initial number of seeded cells per well.

701

29

702   **Bulk RNA sequencing and data analysis.** Four independent sorts of 4T1-Sca-1$^+$ and

703   4T1-Sca-1$^-$ cells (as described in the magnetic cell sorting section) or four independent 4T1

704   cells primed with Tu- Gr1$^+$CD11b$^+$ or Spl-Gr1$^+$CD11b$^+$ were prepared. RNAs of these cells

705   were isolated using the NucleoSpin RNA protocol of Macherey-Nagel (as described in real-

706   time (RT) qPCR and primers section). Samples were normalized for 1 µg RNA in a volume

707   of 20 µl, sequenced on the NextSeq500 sequencer using the NextSeq 500/550 HT reagent

708   v2 kit (Illumina) at the Swiss Integrative Center for Human Health (SICHH) in Fribourg, or

709   the Lausanne Genomics Technologies Facility (GTF, UNIL) in Lausanne, Switzerland. For

710   data analysis, all sequencing reads were processed for quality control, removal of low

711   quality reads, adaptor sequence and ribosomal RNA by fastqc(0.11.8) (82), multiqc (1.9)

712   (83), Trimmomatic (0.39) (84) and SortMeRNA(2.1) (85) accordingly. The filtered reads

713   were mapped to the reference genome (mm10) using htseq-count (0.6.1) (86) or Salmon

714   (0.99.0) (87). The normalization of the read counts and the analysis of the differential

715   expression between the groups of samples were performed with in R(v4.1.3), a free

716   software environment available at https://www.r-project.org/ using packages DESeq2

717   (v3.15) (88). Pathway enrichment analysis was performed using packages GSVA(1.42.0)

718   (89) and GSEABase(1.56.0) (90) with the input of DESeq2 normalized count numbers

719   using ssgsea method comparing the Hallmark genesets from MSigDB (v7.4.1) (91) with

720   default settings. The significant altered pathways were determined by computing

721   moderated t-statistics and false discovery rates with the limma(3.50.3)(92) for pair-wised

722   comparison. The heatmaps were produced with R package pheatmap(1.0.12)(93) with

723   default settings while pathway hierarchy clustering was performed by similarity based on

724   Euclidean distance and the ward aggregation algorithm. The Sca1 Positive and Sca1

725   Negative signatures were extracted from the top 200 most upregulated or downregulated

726   genes in 4T1-Sca-1$^+$ and 4T1-Sca-1$^-$ RNAseq data, respectively, with the threshold of

727   adjusted p-value <0.05, fold change >1.5 or <-1.5 and average normalized count number

728   >20. For Venn diagram, the genes fulfilling the threshold of adjusted p-value < 0.05, fold

729   change > 1.5 or < -1.5 and average normalized count number >20 are compared. The

730   figures were produced with R package venn (1.10) (94) . Further analysis and figures

731   generation were performed in R using packages tidyverse(1.3.1)(95), ggplot2(3.3.6) (96),

732   circlize(0.4.15) (97), biomaRt(2.50.3) (98, 99), RColorBrewer (1.1-3) (100), clusterProfiler

733   (4.2.2) (101, 102), enrichplot (1.14.2) (103), ggpubr(v0.4.0)(104) ggbreak (0.1.0) (104).

734

735   **Microarray hybridization and data analysis** Experiments were performed as previously

736   described (105). Briefly, triplicates wells of cultured 4T1 and MR13 cells were used for RNA

737   extraction using RNeasy kit (QIAGEN). Probe synthesis and GeneChip Mouse Gene Exon

738   1.0 ST Array (Affymetrix Ltd) hybridization were performed at the GTF, UNIL, Lausanne,

739   Switzerland. Microarray analyses were carried out with R. After quantification of gene

740   expression with robust multi-array normalization (99) using the BioConductor package Affy,

741   (http://www.bioconductor.org/) significance of differential gene expression was determined

742   by computing moderated t-statistics and false discovery rates with the limma package (92).

743   Annotation was based on the genome version NCBI Build 36 (Feb. 2006). The obtained p-

744   values were corrected for multiple testing by calculating estimated false discovery rates

745   (FDR) using the method of Benjamini-Hochberg. Heatmaps were produced by color-coding

746   gene-wise standardized log gene expression levels (mean zero standard deviation one).

747   Probe-sets were shown hierarchically clustered by similarity based on Euclidean distance

748   and the ward aggregation algorithm.

749

750   **Public RNAseq data analysis** The RPKM normalized gene expression data in Ross

751   dataset (GSE150928) from multiple murine models of breast cancer metastasis was

752　obtained from Gene Expression Omnibus (GEO) in the NCBI data repository. The data

753　were analyzed and plot with R package tidyverse(1.3.1)(95), ggplot2 (3.3.6) (96) and

754　ggpubr (v0.4.0) (106). The single-cell RNAseq data in Sebastian dataset (43) was obtained

755　from Dryad data repository (https://doi.org/10.6071/M3238R). The data were analyzed with

756　R package Seurat (3.0) (107). The tumor and different myeloid cell populations were

757　extracted for cell-cell interaction analysis using CellPhondDB (2.0) (44). The identified

758　interaction pairs were extracted and plot using circlize (0.4.15) (97) and ComplexHeatmap

759　(2.11.2) (108). The ligands and receptors annotated in the circular plot were compiled from

760　databases in CellTalkDB(109), SingleCellSignalR (110). To investigate the tumor cell

761　dynamics, datasets for 4T1 (GSE158844 and GSM3502134) and MCF-7 (GSM4681765

762　and GSM5904917) were obtained from GEO. The data were filtered and normalized

763　separately before merging with IntegrateData function included in Seurat. Cell cycle

764　regression was performed according to the standard protocol of Seurat. For MCF-7, due

765　the huge difference of the sample size, 2000 cells were randomly selected from

766　GSM4681765 data, and then merged with GSM5904917. Single-cell trajectories analysis

767　was performed with monocle 3 (111–114) with default settings and the root and start point

768　were selected manually for pseudotime caculation. The GSEA analysis of selected clusters

769　was performed with R package fgsea(115) and the gene rank was calculated with Wilcoxon

770　rank sum test and auROC analysis using wilcoxauc function included in presto package.

771　The Tu-Gr1$^+$CD11b$^+$-induced signature was extracted by comparing gene expression

772　between Tu-Gr1$^+$CD11b$^+$ and Spl-Gr1$^+$CD11b$^+$-educated 4T1 cells with adjusted p-value

773　<0.05, fold change >2, and the top 50 genes were selected.

774

775　**Clinical data analysis.** To validate our finding in clinical data, the human orthologs of

776　murine Tu-Gr1$^+$CD11b$^+$-induced signature genes were used. Conversion from murine to

777 human gene symbols and Entrez IDs was performed with the biomaRt package (2.46.3)

778 (98, 99), using the reference mart https://dec2021.archive.ensembl.org. Molecular

779 Taxonomy of Breast Cancer International Consortium (METABRIC) breast cancer data

780 was downloaded from cBioPortal (116–118) in August 2022, and expression data was log2

781 transformed. Expression values were stratified in two groups by median values. Survival

782 curves were generated using the ggsurvplot function from the survminer package

783 (0.4.9)(106), and were compared between groups using a log-rank test. Survival curves

784 were created using the survfit function from the survival package (3.2.11) (119). Cox

785 proportional hazard regression model was performed through the coxph function of the

786 same package.

787

788 **Statistical analyses.** Unless specified, the data were presented as mean ± SEM from at

789 least 3 independent experiments, unless otherwise indicated. Statistical comparisons

790 were performed by an unpaired Student's t test with a two-tailed distribution, one-way

791 ANOVA analysis of variance with Bonferroni post-test or two-way ANOVA with Tukey's or

792 Dunnett's multiple comparison test using Prism 7.0 GraphPad Software, Inc. or R package

793 ggpubr (v0.4.0)(104).

794

795 **Graphic illustrations**. Illustrative schemes were created with BioRender.com.

796

797 **Data and code availability.** The raw and processed bulk RNAseq data used to generate

798 figures in Figure 3 and Supplemental Figure 5 and microarray data used to generate figures

799 in Figure 7 have been deposited in the GEO database under the access code

800 GSEXXXXXX. The code used for the analyses is open-source and available through with

801 R packages described in methods.

Author contributions

Conceptualization, S.P., Q.L., C.R.; Methodology, S.P., N.F., Q.L., C.R.; Software, A.K., N.F., Q.L.; Validation, S.P., M.B., A.K., Q.L.; Formal analysis, S.P., M.B., A.K., Q.L.; Investigation, S.P., M.B., A.K., O.C., Y-T.H., N.D., L.G., Q.L.; Resources, S.P., M.B., A.K., O.C., N.D., L.G., G.L.; Data Curation, S.P., M.B., A.K., N.D., Q.L., C.R.; Writing – original draft preparation, S.P., Q.L., C.R.; Writing – review and editing, S.P., M.B., A.K., Y-T.H., G.L., N.D., Q.L., C.R.; Visualization, S.P., M.B., A.K., Q.L., C.R.; Supervision, S.P., Q.L., C.R.; Project administration, Q.L., C.R.; Funding acquisition, C.R.

References

1. Fares J, Fares MY, Khachfe HH, Salhab HA, Fares Y. Molecular principles of metastasis: a hallmark of cancer revisited. *Signal Transduct. Target. Ther.* 2020;5(1):1–17.

34

826   2. Valdés-Mora F et al. Single-cell transcriptomics reveals involution mimicry during the

827   specification of the basal breast cancer subtype. *Cell Rep.* 2021;35(2):108945.

828   3. Yang D et al. Lineage tracing reveals the phylodynamics, plasticity, and paths of tumor

829   evolution. *Cell* 2022;185(11):1905-1923.e25.

830   4. Torborg SR, Li Z, Chan JE, Tammela T. Cellular and molecular mechanisms of

831   plasticity in cancer. *Trends Cancer* 2022;8(9):735–746.

832   5. Baccelli I, Trumpp A. The evolving concept of cancer and metastasis stem cells. *J. Cell*

833   *Biol.* 2012;198(3):281–293.

834   6. Lawson DA, Kessenbrock K, Davis RT, Pervolarakis N, Werb Z. Tumour heterogeneity

835   and metastasis at single-cell resolution. *Nat. Cell Biol.* 2018;20(12):1349–1360.

836   7. Celià-Terrassa T, Jolly MK. Cancer Stem Cells and Epithelial-to-Mesenchymal

837   Transition in Cancer Metastasis. *Cold Spring Harb. Perspect. Med.* 2020;10(7):a036905.

838   8. Dagogo-Jack I, Shaw AT. Tumour heterogeneity and resistance to cancer therapies.

839   *Nat. Rev. Clin. Oncol.* 2018;15(2):81–94.

840   9. McDonald K-A et al. Tumor Heterogeneity Correlates with Less Immune Response

841   and Worse Survival in Breast Cancer Patients. *Ann. Surg. Oncol.* 2019;26(7):2191–2199.

842   10. Hata AN et al. Tumor cells can follow distinct evolutionary paths to become resistant

843   to epidermal growth factor receptor inhibition. *Nat. Med.* 2016;22(3):262–269.

844   11. Ramirez M et al. Diverse drug-resistance mechanisms can emerge from drug-tolerant

845   cancer persister cells. *Nat. Commun.* 2016;7(1):10690.

846   12. Oskarsson T, Batlle E, Massagué J. Metastatic stem cells: sources, niches, and vital

847   pathways. *Cell Stem Cell* 2014;14(3):306–321.

848   13. Ye F et al. CD49f Can Act as a Biomarker for Local or Distant Recurrence in Breast

849   Cancer. *J. Breast Cancer* 2017;20(2):142–149.

850   14. Vaillant F et al. The Mammary Progenitor Marker CD61/β3 Integrin Identifies Cancer

851   Stem Cells in Mouse Models of Mammary Tumorigenesis. *Cancer Res.*

852   2008;68(19):7711–7717.

853   15. Li JJ, Tsang JY, Tse GM. Tumor Microenvironment in Breast Cancer—Updates on

854   Therapeutic Implications and Pathologic Assessment. *Cancers* 2021;13(16):4233.

855   16. Ge R, Wang Z, Cheng L. Tumor microenvironment heterogeneity an important

856   mediator of prostate cancer progression and therapeutic resistance. *Npj Precis. Oncol.*

857   2022;6(1):1–8.

858   17. Peng D et al. Myeloid-Derived Suppressor Cells Endow Stem-like Qualities to Breast

859   Cancer Cells through IL6/STAT3 and NO/NOTCH Cross-talk Signaling. *Cancer Res.*

860   2016;76(11):3156–3165.

861   18. Li K et al. Myeloid-derived suppressor cells as immunosuppressive regulators and

862   therapeutic targets in cancer. *Signal Transduct. Target. Ther.* 2021;6(1):1–25.

863   19. Lorusso G, Ruegg C. The tumor microenvironment and its contribution to tumor

864   evolution toward metastasis. *Histochem Cell Biol* 2008;130(6):1091–103.

865   20. Sleeman JP et al. Concepts of metastasis in flux: the stromal progression model.

866   *Semin Cancer Biol* 2012;22(3):174–86.

867   21. Cha YJ, Koo JS. Role of Tumor-Associated Myeloid Cells in Breast Cancer. *Cells*

868   2020;9(8). doi:10.3390/cells9081785

869   22. Pastaki Khoshbin A, Eskian M, Keshavarz-Fathi M, Rezaei N. Roles of Myeloid-

870   Derived Suppressor Cells in Cancer Metastasis: Immunosuppression and Beyond. *Arch*

871   *Immunol Ther Exp Warsz* 2019;67(2):89–102.

872   23. Panni RZ et al. Tumor-induced STAT3 activation in monocytic myeloid-derived

873   suppressor cells enhances stemness and mesenchymal properties in human pancreatic

874   cancer. *Cancer Immunol. Immunother.* 2014;63(5):513–528.

875   24. Cui TX et al. Myeloid-derived suppressor cells enhance stemness of cancer cells by

876   inducing microRNA101 and suppressing the corepressor CtBP2. *Immunity*

877   2013;39(3):611–621.

878   25. Abaurrea A, Araujo AM, Caffarel MM. The Role of the IL-6 Cytokine Family in

879   Epithelial–Mesenchymal Plasticity in Cancer Progression. *Int. J. Mol. Sci.*

880   2021;22(15):8334.

881   26. Zarling JM et al. Oncostatin M: a growth regulator produced by differentiated

882   histiocytic lymphoma cells. *Proc. Natl. Acad. Sci. U. S. A.* 1986;83(24):9739–9743.

883   27. Felcher CM, Bogni ES, Kordon EC. IL-6 Cytokine Family: A Putative Target for

884   Breast Cancer Prevention and Treatment. *Int J Mol Sci* 2022;23(3).

885   doi:10.3390/ijms23031809

886   28. Johnson DE, O'Keefe RA, Grandis JR. Targeting the IL-6/JAK/STAT3 signalling axis

887   in cancer. *Nat Rev Clin Oncol* 2018;15(4):234–248.

888   29. Quintas-Cardama A, Verstovsek S. Molecular pathways: Jak/STAT pathway:

889   mutations, inhibitors, and resistance. *Clin Cancer Res* 2013;19(8):1933–40.

890   30. Tawara K et al. HIGH expression of OSM and IL-6 are associated with decreased

891   breast cancer survival: synergistic induction of IL-6 secretion by OSM and IL-1beta.

892   *Oncotarget* 2019;10(21):2068–2085.

893   31. West NR, Murphy LC, Watson PH. Oncostatin M suppresses oestrogen receptor-α

894   expression and is associated with poor outcome in human breast cancer. *Endocr. Relat.*

895   *Cancer* 2012;19(2):181–195.

896   32. Guo L et al. Stat3-coordinated Lin-28-let-7-HMGA2 and miR-200-ZEB1 circuits

897   initiate and maintain oncostatin M-driven epithelial-mesenchymal transition. *Oncogene*

898   2013;32(45):5272–5282.

899   33. Araujo AM et al. Stromal oncostatin M cytokine promotes breast cancer progression

900   by reprogramming the tumor microenvironment. *J Clin Invest* 2022;132(7).

901   doi:10.1172/JCI148667

902   34. Bryson BL, Junk DJ, Cipriano R, Jackson MW. STAT3-mediated SMAD3 activation

903   underlies Oncostatin M-induced Senescence. *Cell Cycle* 2017;16(4):319–334.

904   35. Taniguchi K, Karin M. IL-6 and related cytokines as the critical lynchpins between

905   inflammation and cancer. *Semin. Immunol.* 2014;26(1):54–74.

906   36. West NR, Murray JI, Watson PH. Oncostatin-M promotes phenotypic changes

907   associated with mesenchymal and stem cell-like differentiation in breast cancer.

908   *Oncogene* 2014;33(12):1485–1494.

37. Ross C et al. Metastasis-Specific Gene Expression in Autochthonous and Allograft Mouse Mammary Tumor Models: Stratification and Identification of Targetable Signatures. *Mol. Cancer Res. MCR* 2020;18(9):1278–1289.

38. Fico F, Bousquenaud M, Rüegg C, Santamaria-Martínez A. Breast Cancer Stem Cells with Tumor- versus Metastasis-Initiating Capacities Are Modulated by TGFBR1 Inhibition. *Stem Cell Rep.* 2019;13(1):1–9.

39. Hanahan D. Hallmarks of Cancer: New Dimensions. *Cancer Discov.* 2022;12(1):31–46.

40. Ouzounova M et al. Monocytic and granulocytic myeloid derived suppressor cells differentially regulate spatiotemporal tumour plasticity during metastatic cascade. *Nat. Commun.* 2017;8(1):14979.

41. Veglia F, Sanseviero E, Gabrilovich DI. Myeloid-derived suppressor cells in the era of increasing myeloid cell diversity. *Nat. Rev. Immunol.* 2021;21(8):485–498.

42. Bronte V et al. Recommendations for myeloid-derived suppressor cell nomenclature and characterization standards. *Nat. Commun.* 2016;7(1):12150.

43. Sebastian A et al. Single-Cell Transcriptomic Analysis of Tumor-Derived Fibroblasts and Normal Tissue-Resident Fibroblasts Reveals Fibroblast Heterogeneity in Breast Cancer. *Cancers* 2020;12(5):1307.

44. Efremova M, Vento-Tormo M, Teichmann SA, Vento-Tormo R. CellPhoneDB: inferring cell–cell communication from combined expression of multi-subunit ligand–receptor complexes. *Nat. Protoc.* 2020;15(4):1484–1506.

930   45. Brandizzi F, Barlowe C. Organization of the ER–Golgi interface for membrane traffic

931   control. *Nat. Rev. Mol. Cell Biol.* 2013;14(6):382–392.

932   46. Chen K et al. Phenotypically supervised single-cell sequencing parses within-cell-

933   type heterogeneity. *iScience* 2021;24(1):101991.

934   47. Yeo SK et al. Single-cell RNA-sequencing reveals distinct patterns of cell state

935   heterogeneity in mouse models of breast cancer. *eLife* 2020;9:e58810.

936   48. Aouad P et al. Epithelial-mesenchymal plasticity determines estrogen receptor

937   positive breast cancer dormancy and epithelial reconversion drives recurrence. *Nat.*

938   *Commun.* 2022;13(1):4975.

939   49. Jin W. Role of JAK/STAT3 Signaling in the Regulation of Metastasis, the Transition of

940   Cancer Stem Cells, and Chemoresistance of Cancer by Epithelial–Mesenchymal

941   Transition. *Cells* 2020;9(1):217.

942   50. Junk DJ et al. Oncostatin M promotes cancer cell plasticity through cooperative

943   STAT3-SMAD3 signaling. *Oncogene* 2017;36(28):4001–4013.

944   51. Naz F, Shi M, Sajid S, Yang Z, Yu C. Cancer stem cells: a major culprit of intra-tumor

945   heterogeneity. *Am. J. Cancer Res.* 2021;11(12):5782–5811.

946   52. Zhang R, Tu J, Liu S. Novel molecular regulators of breast cancer stem cell plasticity

947   and heterogeneity. *Semin Cancer Biol* 2022;82:11–25.

948   53. Qin S et al. Emerging role of tumor cell plasticity in modifying therapeutic response.

949   *Signal Transduct. Target. Ther.* 2020;5(1):228.

950 54. Kong D, Hughes CJ, Ford HL. Cellular Plasticity in Breast Cancer Progression and

951 Therapy. *Front. Mol. Biosci.* 2020;7:72.

952 55. Muzio G, Maggiora M, Paiuzzi E, Oraldi M, Canuto RA. Aldehyde dehydrogenases

953 and cell proliferation. *Free Radic. Biol. Med.* 2012;52(4):735–746.

954 56. Curtis C et al. The genomic and transcriptomic architecture of 2,000 breast tumours

955 reveals novel subgroups. *Nature* 2012;486(7403):346–352.

956 57. Shen M et al. A review of current progress in triple-negative breast cancer therapy.

957 *Open Med Wars* 2020;15(1):1143–1149.

958 58. Al-Mahmood S, Sapiezynski J, Garbuzenko OB, Minko T. Metastatic and triple-

959 negative breast cancer: challenges and treatment options. *Drug Deliv Transl Res*

960 2018;8(5):1483–1507.

961 59. Azim HA, Ghosn M, Oualla K, Kassem L. Personalized treatment in metastatic triple-

962 negative breast cancer: The outlook in 2020. *Breast J* 2020;26(1):69–80.

963 60. Vagia E, Mahalingam D, Cristofanilli M. The Landscape of Targeted Therapies in

964 TNBC. *Cancers Basel* 2020;12(4). doi:10.3390/cancers12040916

965 61. Hua Z, White J, Zhou J. Cancer stem cells in TNBC. *Semin Cancer Biol* 2022;82:26–

966 34.

967 62. Batlle E, Clevers H. Cancer stem cells revisited. *Nat Med* 2017;23(10):1124–1134.

968 63. Brooks MD, Burness ML, Wicha MS. Therapeutic Implications of Cellular

969 Heterogeneity and Plasticity in Breast Cancer. *Cell Stem Cell* 2015;17(3):260–71.

970   64. Yeo SK, Wen J, Chen S, Guan JL. Autophagy Differentially Regulates Distinct Breast

971   Cancer Stem-like Cells in Murine Models via EGFR/Stat3 and Tgfbeta/Smad Signaling.

972   *Cancer Res* 2016;76(11):3397–410.

973   65. Gong J et al. Genotoxic stress induces Sca-1-expressing metastatic mammary

974   cancer cells. *Mol. Oncol.* 2018;12(8):1249–1263.

975   66. Shimokawa M et al. Visualization and targeting of LGR5+ human colon cancer stem

976   cells. *Nature* 2017;545(7653):187–192.

977   67. Oo MW et al. Resident stroma-secreted chemokine CCL2 governs myeloid-derived

978   suppressor cells in the tumor microenvironment. *JCI Insight* 2022;7(1).

979   doi:10.1172/jci.insight.148960

980   68. Franklin DA et al. MEK activation modulates glycolysis and supports suppressive

981   myeloid cells in TNBC. *JCI Insight* 2020;5(15). doi:10.1172/jci.insight.134290

982   69. Bullock K, Richmond A. Suppressing MDSC Recruitment to the Tumor

983   Microenvironment by Antagonizing CXCR2 to Enhance the Efficacy of Immunotherapy.

984   *Cancers Basel* 2021;13(24). doi:10.3390/cancers13246293

985   70. Jovanovic IP et al. Interleukin-33/ST2 axis promotes breast cancer growth and

986   metastases by facilitating intratumoral accumulation of immunosuppressive and innate

987   lymphoid cells. *Int J Cancer* 2014;134(7):1669–82.

988   71. Szczerba BM et al. Neutrophils escort circulating tumour cells to enable cell cycle

989   progression. *Nature* 2019;566(7745):553–557.

72. Doherty MR et al. The opposing effects of interferon-beta and oncostatin-M as regulators of cancer stem cell plasticity in triple-negative breast cancer. *Breast Cancer Res* 2019;21(1):54.

73. Cavalli LR, Riggins RB, Wang A, Clarke R, Haddad BR. Frequent loss of heterozygosity at the interferon regulatory factor-1 gene locus in breast cancer. *Breast Cancer Res. Treat.* 2010;121(1):227–231.

74. Weichselbaum RR et al. An interferon-related gene signature for DNA damage resistance is a predictive marker for chemotherapy and radiation for breast cancer. *Proc. Natl. Acad. Sci. U. S. A.* 2008;105(47):18490–18495.

75. Aljohani AI et al. Myxovirus resistance 1 (MX1) is an independent predictor of poor outcome in invasive breast cancer. *Breast Cancer Res. Treat.* 2020;181(3):541–551.

76. Chan JM et al. Lineage plasticity in prostate cancer depends on JAK/STAT inflammatory signaling. *Science* 2022;377(6611):1180–1191.

77. Deng S et al. Ectopic JAK–STAT activation enables the transition to a stem-like and multilineage state conferring AR-targeted therapy resistance. *Nat. Cancer* 2022;3(9):1071–1087.

78. Lynce F et al. Phase I study of JAK1/2 inhibitor ruxolitinib with weekly paclitaxel for the treatment of HER2-negative metastatic breast cancer. *Cancer Chemother Pharmacol* 2021;87(5):673–679.

79. Kearney M et al. Phase I/II trial of ruxolitinib in combination with trastuzumab in metastatic HER2 positive breast cancer. *Breast Cancer Res Treat* 2021;189(1):177–185.

80. O'Shaughnessy J et al. A randomized, double-blind, phase 2 study of ruxolitinib or placebo in combination with capecitabine in patients with advanced HER2-negative breast cancer and elevated C-reactive protein, a marker of systemic inflammation. *Breast Cancer Res Treat* 2018;170(3):547–557.

81. Lan Q et al. Type I interferon/IRF7 axis instigates chemotherapy-induced immunological dormancy in breast cancer. *Oncogene* 2019;38(15):2814–2829.

82. FASTQC. A quality control tool for high throughput sequence data | BibSonomy [Internet]https://www.bibsonomy.org/bibtex/f230a919c34360709aa298734d63dca3. cited October 15, 2022

83. Ewels P, Magnusson M, Lundin S, Käller M. MultiQC: summarize analysis results for multiple tools and samples in a single report. *Bioinformatics* 2016;32(19):3047–3048.

84. Bolger AM, Lohse M, Usadel B. Trimmomatic: a flexible trimmer for Illumina sequence data. *Bioinformatics* 2014;30(15):2114–2120.

85. Kopylova E, Noé L, Touzet H. SortMeRNA: fast and accurate filtering of ribosomal RNAs in metatranscriptomic data. *Bioinforma. Oxf. Engl.* 2012;28(24):3211–3217.

86. Anders S, Pyl PT, Huber W. HTSeq—a Python framework to work with high-throughput sequencing data. *Bioinformatics* 2015;31(2):166–169.

87. Patro R, Duggal G, Love MI, Irizarry RA, Kingsford C. Salmon provides fast and bias-aware quantification of transcript expression. *Nat. Methods* 2017;14(4):417–419.

88. Love MI, Huber W, Anders S. Moderated estimation of fold change and dispersion for RNA-seq data with DESeq2. *Genome Biol.* 2014;15(12):550.

1032   89. Hänzelmann S, Castelo R, Guinney J. GSVA: gene set variation analysis for

1033   microarray and RNA-Seq data. *BMC Bioinformatics* 2013;14(1):7.

1034   90. Morgan M, Falcon S, Gentleman R. GSEABase: Gene set enrichment data structures

1035   and methods. R package version 1.58.0.2022;

1036   91. Subramanian A et al. Gene set enrichment analysis: A knowledge-based approach

1037   for interpreting genome-wide expression profiles. *Proc. Natl. Acad. Sci.*

1038   2005;102(43):15545–15550.

1039   92. Ritchie ME et al. limma powers differential expression analyses for RNA-sequencing

1040   and microarray studies. *Nucleic Acids Res.* 2015;43(7):e47.

1041   93. Kolde R. Pheatmap: pretty heatmaps. *R Package Version* 2012;1(2):726.

1042   94. Dusa, Adrian. Draw Venn Diagrams R package venn2016;

1043   95. Wickham H et al. Welcome to the Tidyverse. *J. Open Source Softw.* 2019;4(43):1686.

1044   96. Wickham H. *ggplot2 [Internet]*. New York, NY: Springer; 2009:

1045   97. Gu Z, Gu L, Eils R, Schlesner M, Brors B. circlize Implements and enhances circular

1046   visualization in R. *Bioinforma. Oxf. Engl.* 2014;30(19):2811–2812.

1047   98. Durinck S et al. BioMart and Bioconductor: a powerful link between biological

1048   databases and microarray data analysis. *Bioinforma. Oxf. Engl.* 2005;21(16):3439–3440.

1049   99. Durinck S, Spellman PT, Birney E, Huber W. Mapping identifiers for the integration of

1050   genomic datasets with the R/Bioconductor package biomaRt. *Nat. Protoc.*

1051   2009;4(8):1184–1191.

1052   100. Neuwirth E. RColorBrewer: ColorBrewer Palettes:5.

1053 101. Wu T et al. clusterProfiler 4.0: A universal enrichment tool for interpreting omics

1054 data. *Innov. Camb. Mass* 2021;2(3):100141.

1055 102. Yu G, Wang L-G, Han Y, He Q-Y. clusterProfiler: an R package for comparing

1056 biological themes among gene clusters. *Omics J. Integr. Biol.* 2012;16(5):284–287.

1057 103. Yu G, Hu E. enrichplot: Visualization of Functional Enrichment Result [Internet]2022;

1058 doi:10.18129/B9.bioc.enrichplot

1059 104. Xu S et al. Use ggbreak to Effectively Utilize Plotting Space to Deal With Large

1060 Datasets and Outliers. *Front. Genet.* 2021;12:774846.

1061 105. Monnier Y et al. CYR61 and alphaVbeta5 integrin cooperate to promote invasion

1062 and metastasis of tumors growing in preirradiated stroma. *Cancer Res.*

1063 2008;68(18):7323–7331.

1064 106. Kassambara A. ggpubr: "ggplot2" Based Publication Ready Plots

1065 [Internet]2020;https://CRAN.R-project.org/package=ggpubr. cited October 15, 2022

1066 107. Stuart T et al. Comprehensive Integration of Single-Cell Data. *Cell*

1067 2019;177(7):1888-1902.e21.

1068 108. Gu Z, Eils R, Schlesner M. Complex heatmaps reveal patterns and correlations in

1069 multidimensional genomic data. *Bioinforma. Oxf. Engl.* 2016;32(18):2847–2849.

1070 109. Shao X et al. CellTalkDB: a manually curated database of ligand–receptor

1071 interactions in humans and mice. *Brief. Bioinform.* 2021;22(4):bbaa269.

1072 110. Cabello-Aguilar S et al. SingleCellSignalR: inference of intercellular networks from

1073 single-cell transcriptomics. *Nucleic Acids Res.* 2020;48(10):e55.

1074 111. Trapnell C et al. The dynamics and regulators of cell fate decisions are revealed by

1075 pseudotemporal ordering of single cells. *Nat. Biotechnol.* 2014;32(4):381–386.

1076 112. Qiu X et al. Reversed graph embedding resolves complex single-cell trajectories.

1077 *Nat. Methods* 2017;14(10):979–982.

1078 113. Cao J et al. The single-cell transcriptional landscape of mammalian organogenesis.

1079 *Nature* 2019;566(7745):496–502.

1080 114. McInnes L, Healy J, Melville J. UMAP: Uniform Manifold Approximation and

1081 Projection for Dimension Reduction [Internet]2020;http://arxiv.org/abs/1802.03426. cited

1082 October 21, 2022

1083 115. Korotkevich G et al. Fast gene set enrichment analysis [Internet]2021;060012.

1084 116. Gao W et al. IL20RA signaling enhances stemness and promotes the formation of

1085 an immunosuppressive microenvironment in breast cancer. *Theranostics*

1086 2021;11(6):2564–2580.

1087 117. Cerami E et al. The cBio cancer genomics portal: an open platform for exploring

1088 multidimensional cancer genomics data. *Cancer Discov.* 2012;2(5):401–404.

1089 118. Ramos M et al. Multiomic Integration of Public Oncology Databases in

1090 Bioconductor. *JCO Clin. Cancer Inform.* 2020;(4):958–971.

1091 119. Therneau TM, Grambsch PM. *Modeling Survival Data: Extending the Cox Model*

1092 *[Internet]*. New York, NY: Springer; 2000:

1093

1094
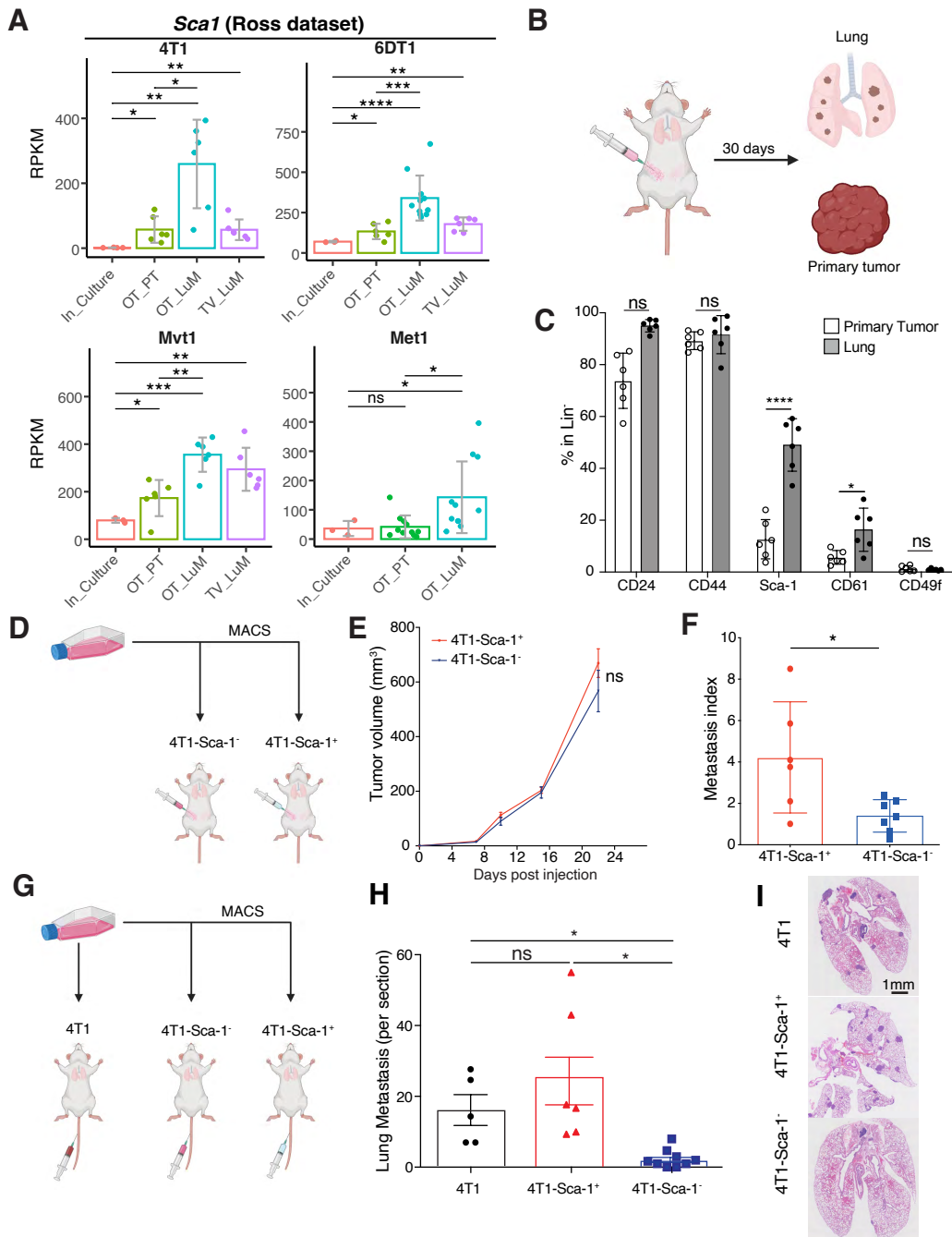
Figure 1. Sca-1+ population is enriched during in vivo metastasis across multiple breast cancer models
(**A**) *Sca-1* mRNA expression in the metastatic murine breast cancer models 4T1, 6DT1, Mvt1 and Met1, extracted from the Ross dataset. Analyzed samples consist of cultured cells (In_Culture), orthotopic injected primary tumors (OP_PT), spontaneous lung metastases (OP_LuM) and lung metastases induced by tail-vain injection (TV_LuM). Data are presented as mean of Reads Per Kilobase of transcript per Million mapped reads (RPKM) ± SD (unpaired two-tailed student's t test with Holm correction).
(**B**) Experimental set up for *in vivo* experimental validation. The 4T1 tumor cells were orthotopically injected into the 4th mammary fat pad. Thirty days later, cells from primary tumors and lungs were isolated to examine CSC marker expression by flow cytometry.
(**C**) Frequency of CSC marker expression in primary tumors and lung metastases. Results give the percentage of CD24, CD44, Sca-1, CD61 and CD49f positive cells gated in lineage negative cells (CD45⁻CD31⁻TER119⁻).
(**D-F**) Experimental set up (**D**) of the in vivo experiment to assess tumor growth (e) and lung metastatic ability (metastatic index) (**F**) of 4T1-Sca-1⁺ and 4T1-Sca-1⁻ populations isolated from parental 4T1 cells orthotopically injected into the 4th mammary fat pad. Metastases are assessed 21 days after tumor cell injection. n=8/group, 3 independent experiments.
(**G-I**) Experimental set up (**G**) of the in vivo experiment to assess lung colonization capacity of sorted parental 4T1, 4T1-Sca-1⁺ and 4T1-Sca-1⁻ cells by tail-vain injection. Lung metastatic nodule numbers (**H**) and representative images (**I**) of lungs from mice 10 days post injection (n=5-6, 2 independent experiments). Scale bar=1 mm. Except **A**, data are represented as mean values ± SEM. P values were calculated using unpaired two-tailed student's t test with Holm correction (**A**), unpaired two-tailed student's t test (**C, F**), two-way ANOVA with Tukey multiple-comparison test (**E**) or one-way ANOVA with Tukey multiple-comparison test (**H**). *, p<0.05; **, p< 0.01; ***, p< 0.001; ****, p< 0.0001; ns, non-significant.
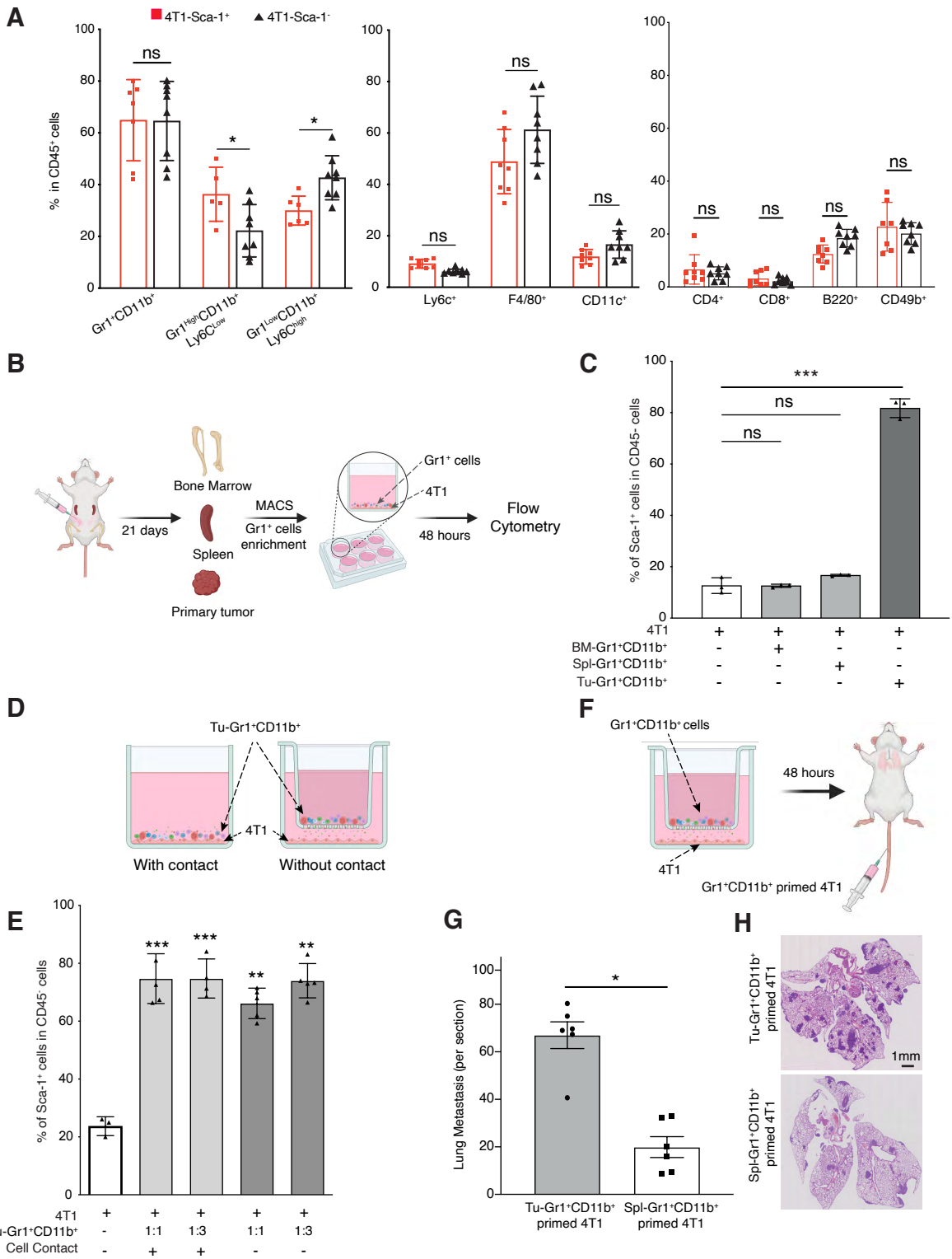
Figure 2. Sca-1 expression is modulated by the tumor microenvironment

Figure 2. Sca-1 expression is modulated by the tumor microenvironment

(A) Frequency of different immune cell populations in primary tumors of mice orthotopically injected with 4T1-Sca-1$^+$ and 4T1-Sca-1$^-$ 21 days post injection. Populations are determined in CD45 negative, viable cells (n=8 mice/Group).

(B-C) Illustrative scheme **(B)** showing the experimental design for isolating Gr1$^+$ cells from different sites of tumor-bearing mice. Twenty-one days after tumor implantation, Gr1$^+$ cells were isolated from bone marrow (BM-Gr1+CD11b+), spleen (Spl- Gr1+CD11b+) or primary tumor (Tu-Gr1$^+$CD11b$^+$) and co-cultured for 48 hours with parental 4T1 cells in vitro. Sca-1 expression in tumor cells was examined by flow cytometry **(C)**. Co-cultures conditions are indicated in the bar graph (n=3/group).

(D) Illustrative scheme of the experimental co-culture setup.

(E) MACS-enriched Gr1$^+$ cells were cocultured with 4T1 cells with or without Transwell inserts of 0.4 μm pore size. The 4T1 cells were seeded in the bottom well and Gr1$^+$CD11b$^+$ cells in the upper part of the insert. After 48 hours, 4T1 cells were examined for Sca1 expression by FACS. Co-cultures conditions are indicated in the bar graph. The ratio of tumor cells and Tu-Gr1$^+$CD11b$^+$ is varied from 1:1 to 1:3. Significant enrichment of Sca-1$^+$ population were observed in all conditions. n= 3-5/group.

(F) Illustrative scheme of the experimental metastasis setup.

(G-H) Evaluation of the metastatic capacity of Gr1$^+$CD11b$^+$-educated 4T1 cells in vivo. The 4T1 tumor cells were primed with Tu-Gr1$^+$CD11b$^+$ or Spl-Gr1$^+$CD11b$^+$ in vitro without cell-cell contact for 48 hours and injected into the tail vein of mice. Lung metastases were quantified 10 days after injection **(G)**, and representative H&E staining images of lung sections are showed **(H)**. Scale bar=1mm, n=7 mice/group.

Data are represented as mean values ± SEM from at least 3 independent experiments. P values were calculated using unpaired two-tailed student's t test **(A, G)**, one-way ANOVA with Dunnett's multiple-comparison test **(C, E)**. *, p<0.05; **, p< 0.01; ***, p< 0.001; ns, non-significant.
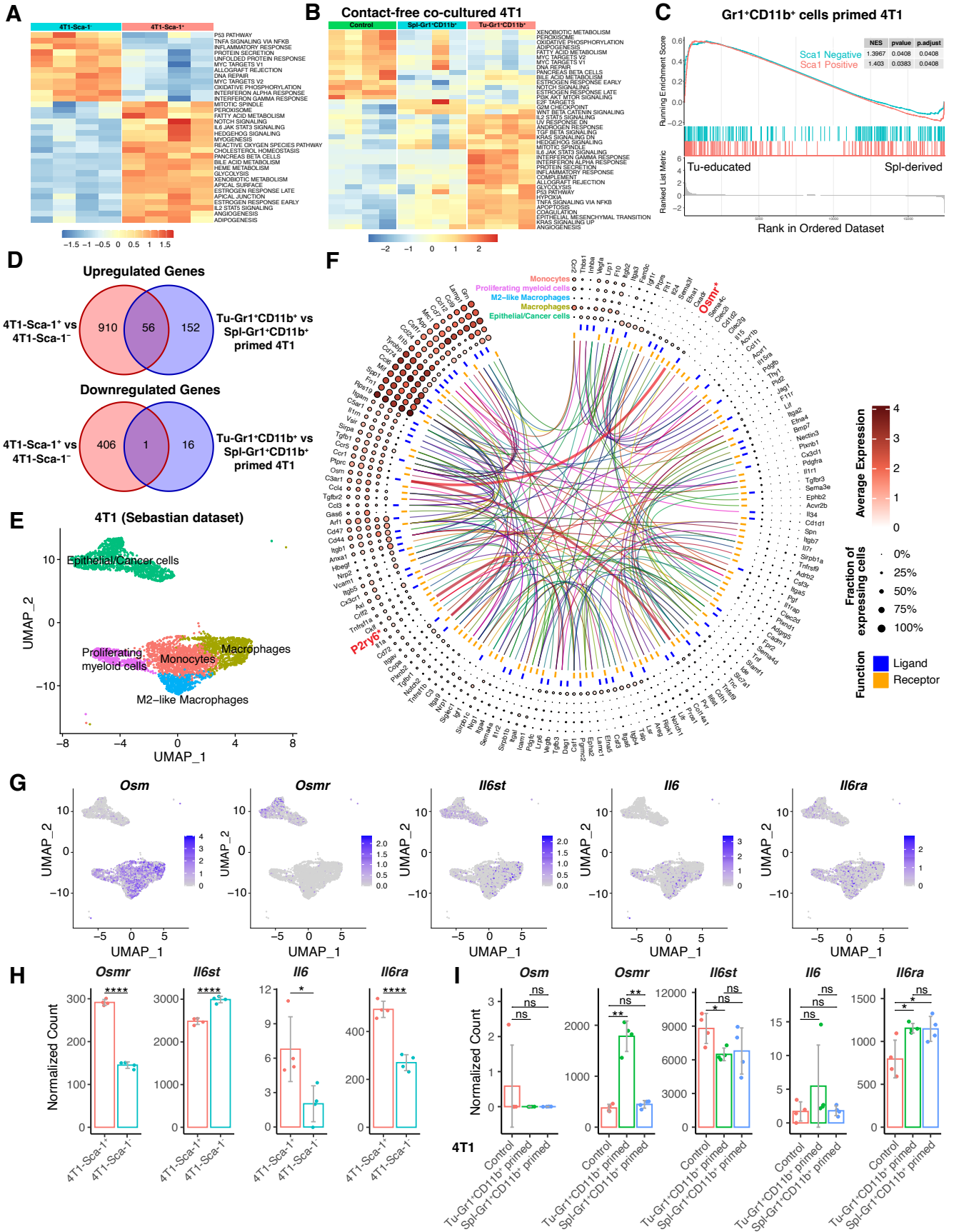
Figure 3. Transcriptomic analysis of Sca-1+ tumor cells

Figure 3. Transcriptomic analysis of Sca-1$^+$ tumor cells

(A) Heatmap showing the signature score of the hallmark pathways analysis in 4T1-Sca-1$^+$ and 4T1-Sca-1$^-$ population sorted from parental 4T1 cells. The colors code the expression levels relative to average levels as indicate at the bottom.

(B) Heatmap showing the signature score of the hallmarks pathway analysis in parental 4T1 (4T1), Spl-Gr1$^+$CD11b$^+$ primed 4T1 and Tu-Gr1$^+$CD11b$^+$ primed 4T1 cells. The colors code the expression levels relative to average levels as indicate at the bottom.

(C) Gene set enrichment analysis (GSEA) comparing the Tu-Gr1$^+$CD11b$^+$ and Spl-Gr1$^+$CD11b$^+$ primed 4T1 cells. GSEA shows positive correlations of both Sca1 Positive and Sca1 Negative signatures. NES, normalized enrichment score.

(D) Venn diagrams showing that 56 upregulated genes, and 1 downregulated gene are shared between endogenous and Tu-Gr1$^+$CD11b$^+$ induced Sca-1$^+$ population in 4T1 tumor cells.

(E) UMAP plot showing clusters of cancer cells and myeloid cell populations in orthotopically growing 4T1-derived primary tumors extracted from the Sebastian dataset (see Materials and Methods for details).

(F) Circos diagram showing the potential interactions between cancer cells and different myeloid cell populations determined by CellPhoneDB (see Materials and Methods for details) based on the Sebastian dataset. Only OSMR and P2RY6 are shared with the common 56 gene list showed in panel **D**.

(G) UMAP plot showing the gene expression pattern of *Osm*, *Osmr*, *Il6st*, *Il6* and *Il6ra* in different cell populations in the Sebastian dataset.

(H-I) mRNA expression of *Osm*, *Osmr*, *Il6st*, *Il6* and *Il6ra* based on RNAseq data used to generate the heatmaps shown in **A** & **B**, respectively. *Osm* expression is not detected in sorted 4T1 cells.

Data are presented as mean of normalized count ± SD. P values: *, $p<0.05$; **, $p< 0.01$; ***, $p< 0.001$; ****, $p< 0.0001$; ns, non-significant (unpaired two-tailed student's t test for **H**, and unpaired two-tailed student's t test with Holm correction for **I**).
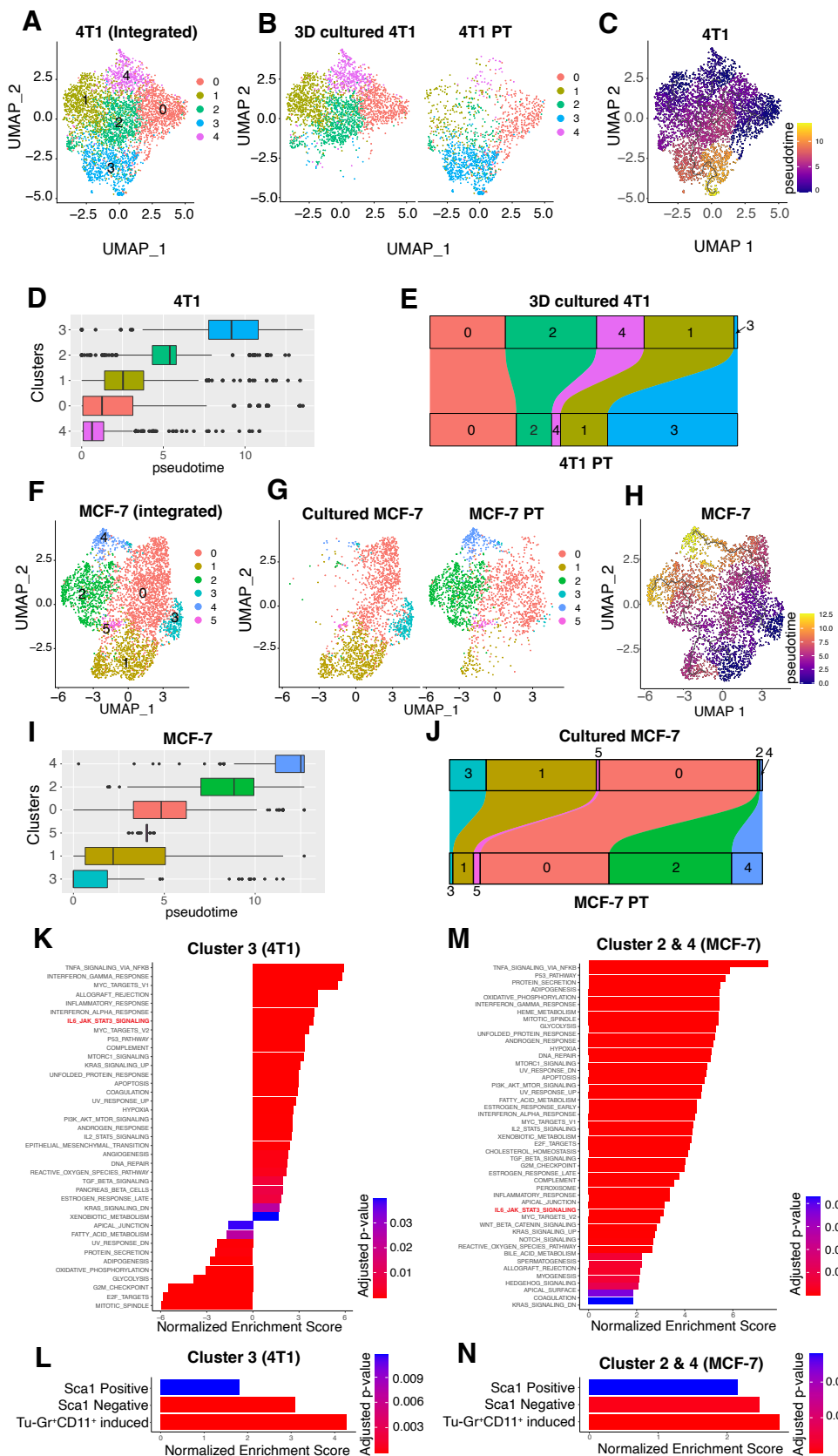
Figure 4. Transformation dynamics of tumor cell populations induced by the tumor microenvironment

Figure 4. Transformation dynamics of tumor cell populations induced by the tumor microenvironment

(A) UMAP plots showing 4T1 clusters based on integrated scRNA-seq data from 4T1 cells in 3D culture or in primary tumor.

(B) Distribution of specific clusters in 4T1 cells in 3D culture or in primary tumor (PT).

(C-D) UMAP plot **(C)** and boxplot **(D)** showing the clusters in pseudo-time during the transformation of 4T1 cells from *ex vivo* culture to *in vivo*.

(E) Sankey diagram showing the dynamic of each cluster during the transformation of 4T1 cells from *ex vivo* culture to in vivo. Cluster 3 was largely expanded *in vivo*.

(F) UMAP plots showing MCF-7 clusters based on integrated scRNA-seq data from MCF-7 cells in culture or in primary tumor.

(G) Distribution of the specific clusters in cultured MCF7 cells or in MCF7 primary tumors (PT).

(H-I) UMAP plot **(H)** and boxplot **(I)** showing the clusters in pseudo-time during the transformation of MCF-7 cells from *ex vivo* culture to *in vivo*.

(J) Sankey diagram showing the dynamic of each cluster during the transformation of MCF-7 cells from *ex vivo* culture to *in vivo*. Cluster 2 and 4 were largely expanded *in vivo*.

(K-L) GESA analysis of Hallmark gene sets **(K)** and Sca1 Positive signature, Sca1 Negative Signature and Tu-Gr1$^+$CD11b$^+$ induced signature **(L)** of cluster 3 in 4T1 data. Only the signatures with adjusted p-value <0.05 were shown.

(M-N) GESA analysis of Hallmark gene sets (M) and Sca1 Positive signature, Sca1 Negative Signature and Tu-Gr1$^+$CD11b$^+$ induced signature **(N)** of cells in cluster 2 or cluster 4 in MCF-7 data. Only the signatures with adjusted p-value <0.05 were shown.

Analyses are based on publicly available data (4T1: GSM4812003 and GSM3502134; MCF-7: GSM4681765 and GSM5904917).
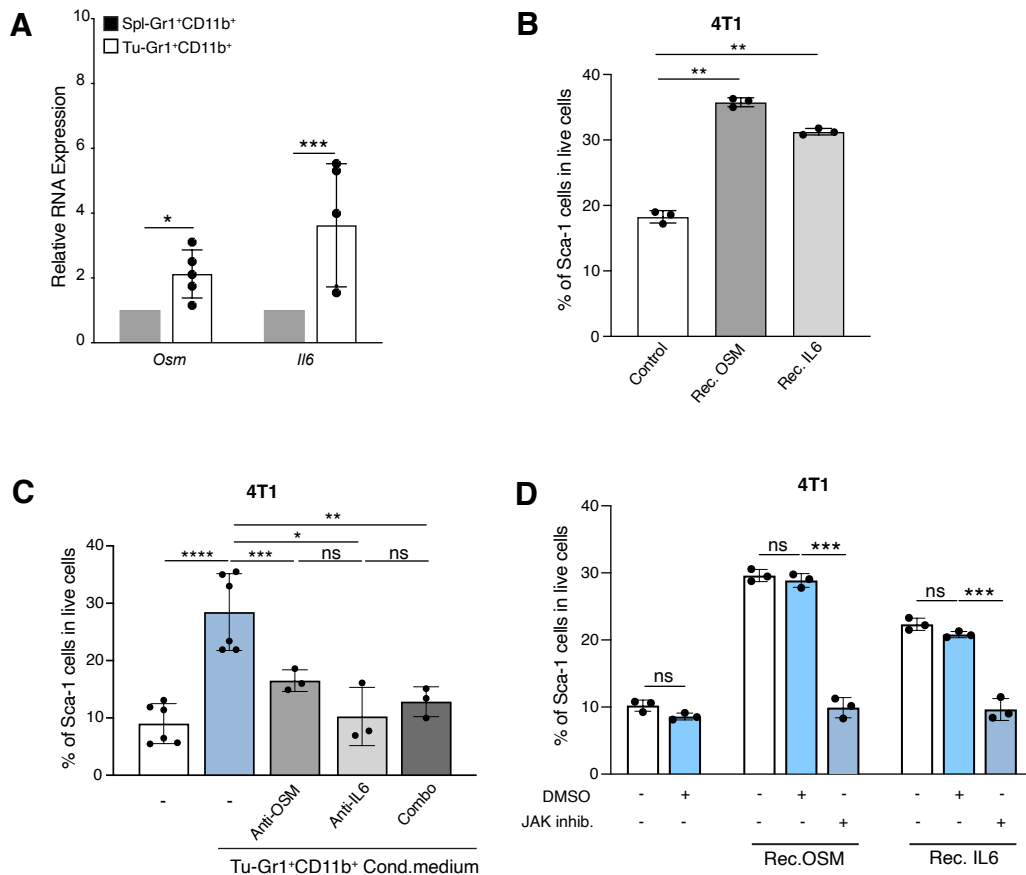
Figure 5. Sca-1+ population is modulated by the OSM/IL6-JAK pathway

(**A**) Quantitative PCR analysis of *Osm* and *Il6* mRNA expression in Tu-Gr1+CD11b+ and Spl- Gr1+CD11b+. Tu-Gr1+CD11b+ express significantly higher *Osm* and *Il6* levels compared with Spl-Gr1+CD11b+. n = 4-5/group.

(**B**) Fraction of 4T1-Sca1+ cells upon exposure to recombinant Il6 or Osm protein (1 μg/ml for 48 hours) as determined by flow cytometry. Both cytokines induced the Sca-1+ population in cultured 4T1 tumor cells. n = 3/group.

(**C**) Inhibition of OSM and IL6 from Tu-Gr1+CD11b+ conditioned medium with anti-OSM or anti-IL6 neutralizing antibody as indicated. Treatment with either antibody significantly suppressed the Sca-1+ population enrichment. n = 3-6/group.

(**D**) Treatment with the JAK inhibitor Ruxolitinib (5 μM) of cultured 4T1 cells stimulated with recombinant IL6 or OSM protein (1 μg/ml, 48 hours exposure) as indicated. Ruxolitinib inhibited Sca-1+ population enrichment induced by recombinant IL6 or OSM protein. n = 3/group. Data are represented as mean ± SEM from 3 independent experiments. *, $p<0.05$; **, $p< 0.01$; ***, $p< 0.001$; ****, $p< 0.0001$; ns, non-significant (unpaired two-tailed student's t test for **A**, and one-way ANOVA with Dunnett's multiple-comparison test for **B** and **D**, and one-way ANOVA with Tukey multiple-comparison test for **C**).
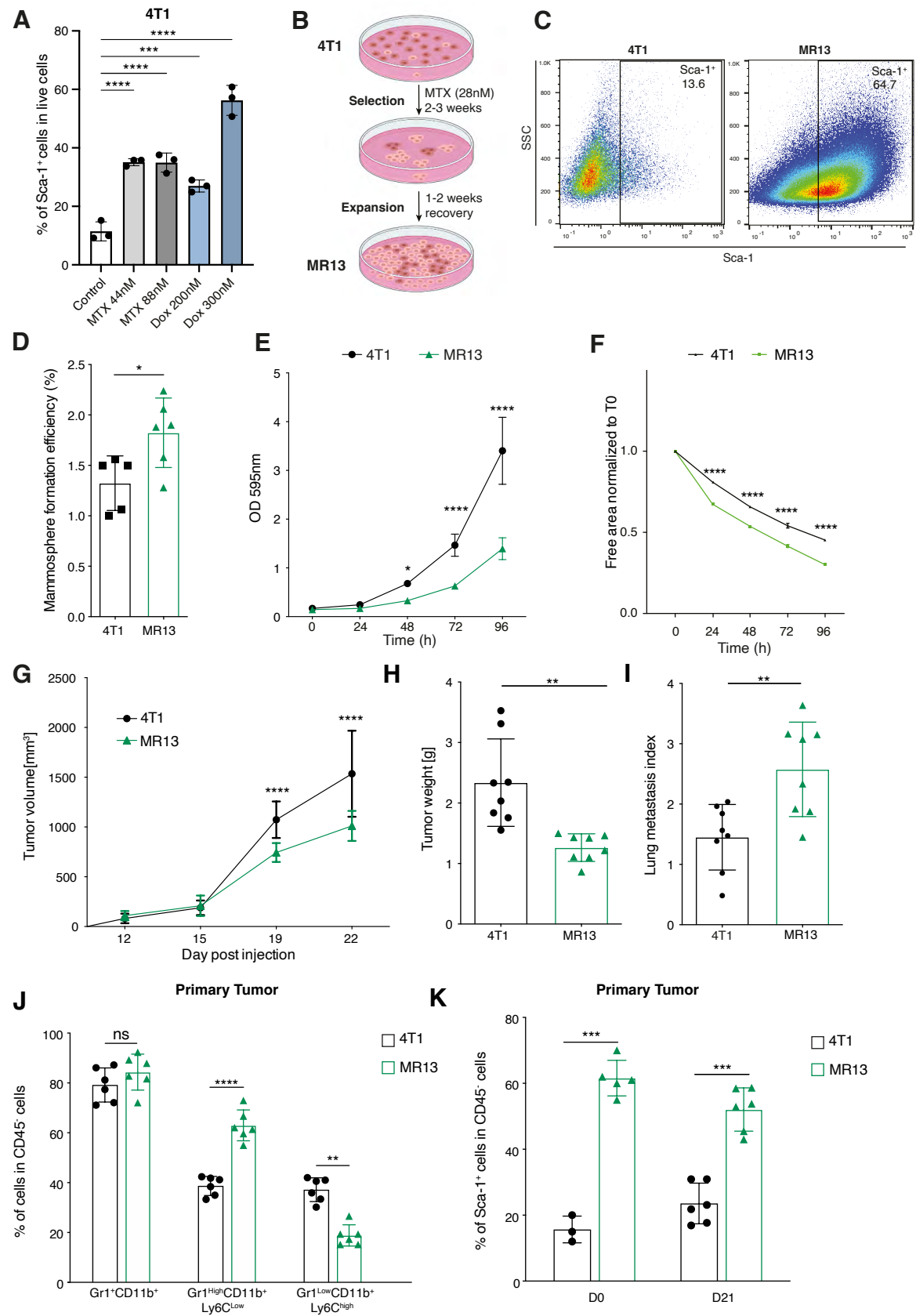
Figure 6. Long term chemotherapy treatment of 4T1 cells induces a stable Sca-1+ population (MR13) with higher metastatic capacity and CSC features

Figure 6. Long term chemotherapy treatment of 4T1 cells induces a stable Sca-1⁺ population (MR13) with higher metastatic capacity and CSC features

(A) Fraction of 4T1-Sca1⁺ cells upon short-term (48 hours) Methotrexate (44 and 88 nM) and Doxorubicin (200 and 300 nM) treatments. All treatments induced enrichment of Sca-1⁺ population. n = 3/group.

(B) Illustrative scheme of the experimental design to obtain chemotherapy resistant MR13 cells from 4T1.

(C) Dot plots representing Sca-1 expression vs SSC determined by flow cytometry in MR13 chemotherapy resistant cells vs parental 4T1 tumor cells in vitro.

(D) Quantification of the mammosphere forming efficiency of 4T1 and MR13 tumor cells. n = 5-6/group.

(E) Cell proliferation curve of 4T1 and MR13 tumor cells in vitro determined by crystal violet assay. The results are presented as mean of optical density (OD). n = 8/group.

(F) Cell motility of 4T1 and MR13 tumor cells determined by a scratch wound healing assay. n=5-6/group. Results are presented as cell-free area relative to the initial wound area from 3 independent experiments.

(G) Growth curves of primary tumors in BALB/c mice orthotopically injected with 4T1 and MR13 tumor cells (n=10-11/group).

(H) Tumor weight of 4T1 and MR13 tumors recovered from BALB/c mice at day 22 post injection (n=8-9/group).

(I) Lung metastasis index 23 days post injection. The number of metastatic nodules is determined by H&E staining and normalized based on the primary tumor weight (n=8-9/group).

(J) Frequency of different CD11b⁺ myeloid cells subpopulations in primary tumors from MR13 and 4T1 injected mice determined by flow cytometry 21-days post injection (n= 6). Subpopulations are determined in CD45 positive, viable cell population.

(K) Percentage of Sca-1⁺ tumor cells at time of injections (D0) of 4T1 and MR13 cells and in primary tumors recovered at day 21 (D21). Sca-1 expression is determined in CD45 negative, viable cell population. n = 3-6/group.

Data are represented as mean ± SEM from at least 3 independent experiments. *, $p<0.05$; **, $p< 0.01$; ***, $p< 0.001$; ****, $p< 0.0001$; ns, non-significant (one-way ANOVA with Dunnett's multiple-comparison test for **A**, unpaired two-tailed student's t test for **D**, **H-K**, and two-way ANOVA with Tukey's multiple comparison test for **E-G**).
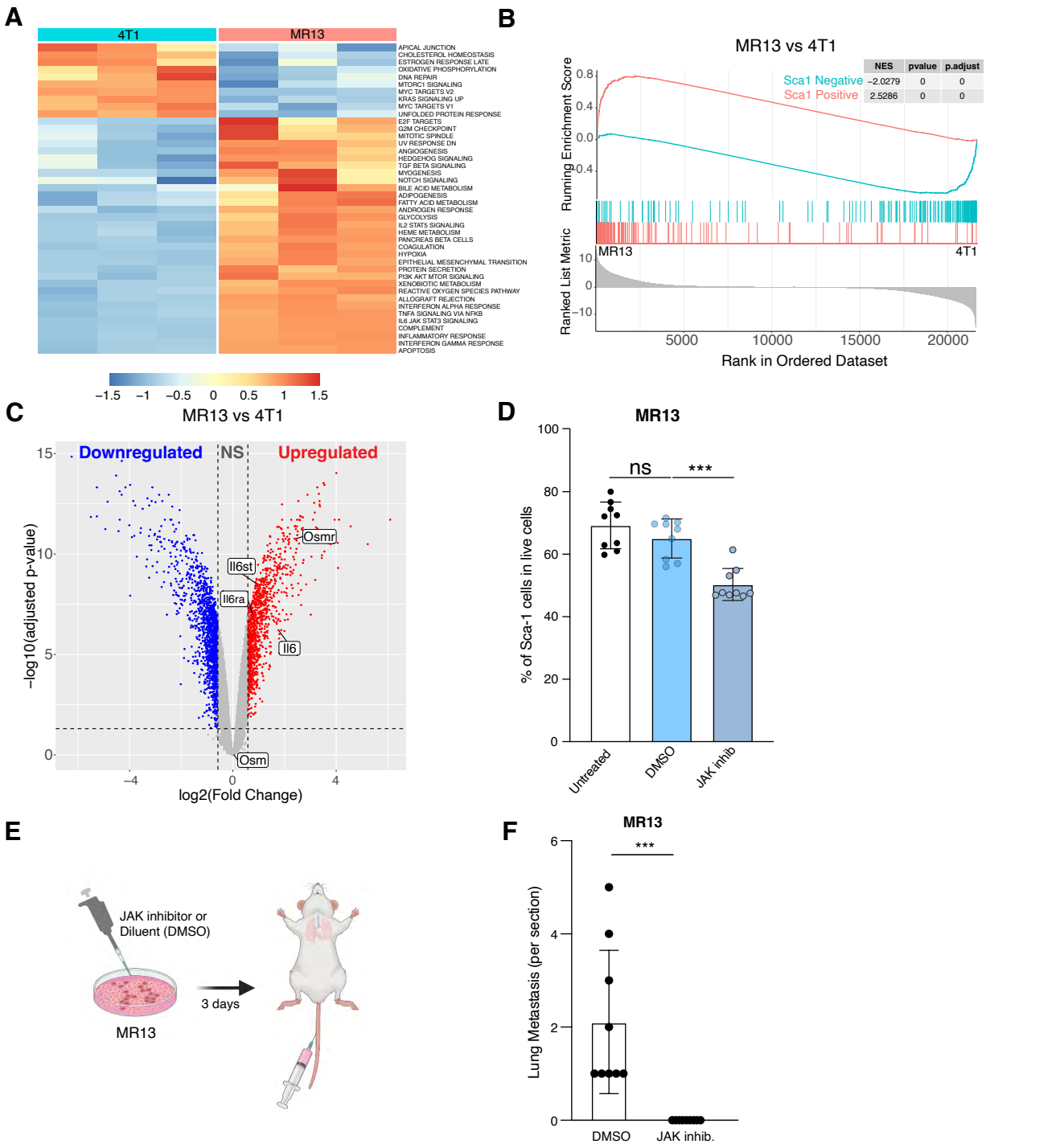
Figure 7. IL6-JAK pathway promotes Sca-1^{+} persistence and metastatic capacity in chemotherapy resistant MR13 tumor cells
(A-B) Gene expression analysis of parental 4T1 and chemotherapy resistant MR13 cells. Heat map represents the signature score of the hallmark pathways analysis. Results from 3 biological replicates are shown **(A)**. GSEA results showing that MR13 cells are positively enriched with for the Sca1 Positive signature and negatively with for the Sca1 Negative signature **(B)**.
(C) Volcano plot showing the differential expression of *Osm*, *Osmr*, *Il6st*, *Il6* and *Il6ra* mRNA in MR13 vs 4T1 tumor cells.
(D) Fraction of Sca-1^{+} population in MR13 tumor cells treated for 48 hours with Ruxolitinib (5 µM) relative to vehicle control (DMSO) treatment.
(E) Illustrative scheme of the experimental design for testing the effect of Ruxolitinib on MR13 metastatic capacity shown in F. MR13 tumor cells were treated with Ruxolitinib or DMSO in vitro for 72 hours and then injected into the mice tail vein. Lungs were examined for metastasis 10 days after tumor cell injection.
(F) Number of metastatic nodules in the lungs from mice injected with MR13 treated in vitro with Ruxolitinib or DMSO and indicated (n=9/group).
Data are represented as mean values ± SEM from 3 independent experiments. P values: ns, non-significant, ***< 0.001 (one-way ANOVA with Dunnett's multiple-comparison test for **D**, and unpaired two-tailed student's t test for **F**).
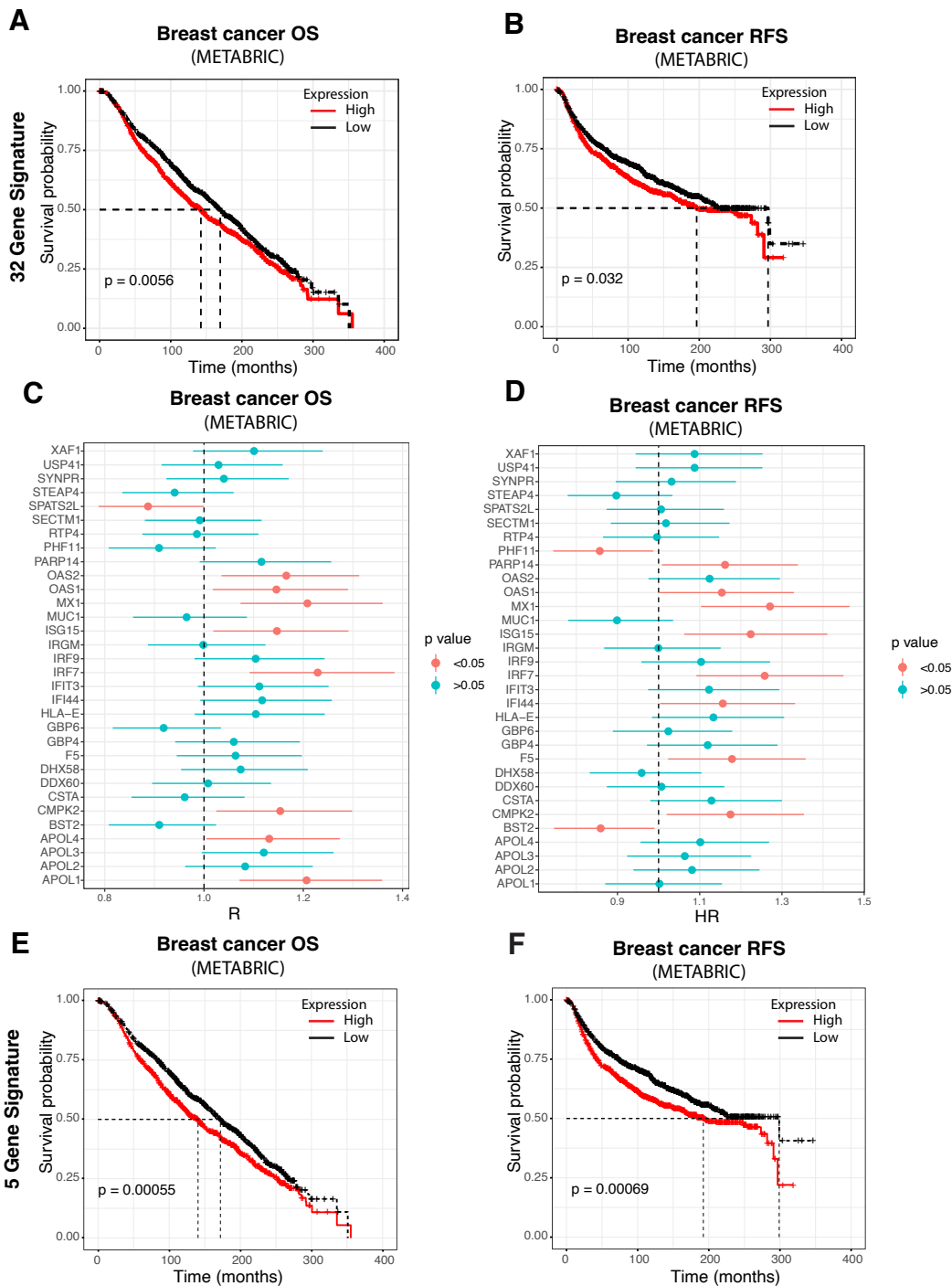
Figure 8. Tu-Gr1⁺CD11b⁺-induced tumor cell signature predicts worse outcome in breast cancer patients

(**A-B**) Kaplan-Meier curves showing overall survival (OS) (**A**) or relapse-free survival (RFS) (**B**) for breast cancer patients according to high or low expression of an orthologue 32 gene signature, based on the Tu-Gr1⁺CD11b⁺-induced 4T1 cell signature, in the METABRIC datasets.

(**C-D**) Forest plots showing the Cox proportional hazard regression (HR) for OS (**C**) and RFS (**D**) of the individual 32 orthologues of the Tu-Gr1⁺CD11b⁺-induced signature, based on gene expression in tumor samples from METABRIC dataset.

(**E-F**) Kaplan-Meier curves showing OS (**E**) and RFS (**F**) according to the reduced 5 orthologue gene signature expression in the METABRIC datasets.

The p value for **A**, **B**, **E**, **F** was calculated using the log-rank test and high and low expression levels were stratified by median values.
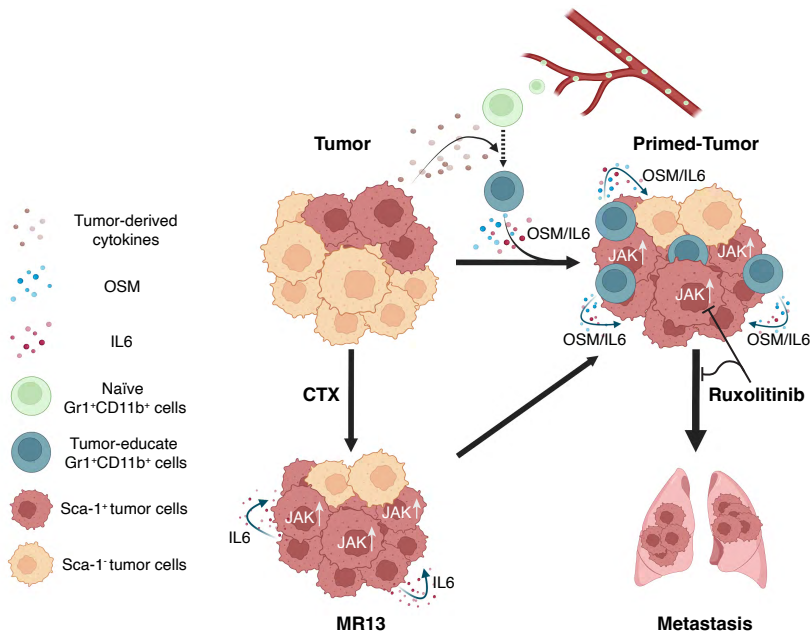
Figure 9 Illustrative scheme of the proposed model for cancer cell plasticity modulated by OSM/IL6 during tumor progression and chemotherapy

Parental tumor cells maintain a small portion of highly metastatic Sca-1+ population. During tumor progression, naïve Gr1+CD11b+ are recruited to the TME and educated into Tu-Gr1+CD11b+ by tumor-derived factors. In turn, Tu-Gr1+CD11b+ secrete OSM and IL6 to convert Sca-1- population into a highly metastatic Sca-1+ population. Chemotherapy (CTX) enriched for Sca-1+ population due to its intrinsic resistance against cytotoxic treatment. Resistant cells express IL6 to maintain the high portion of Sca-1+ population with high metastatic ability. JAK inhibitor Ruxolitinib suppresses the conversion to Sca-1+ population and metastasis. Inhibition of OSM, IL6 and the activated downstream kinase JAK are candidate therapeutic targets to impinge on metastatic breast cancer progression during natural evolution and following therapy-resistance.